Implementation of a discontinuous Galerkin morphological model on two-dimensional unstructured meshes

C. Mirabito [a,*], C. Dawson [a], E.J. Kubatko [b], J.J. Westerink [c], S. Bunya [d]

[a] Institute for Computational Engineering and Sciences, The University of Texas at Austin, Austin, TX 78712, USA
[b] Department of Civil and Environmental Engineering and Geodetic Science, The Ohio State University, Columbus, OH 43210, USA
[c] Environmental Fluid Dynamics Laboratories, Department of Civil Engineering and Geological Sciences, University of Notre Dame, Notre Dame, IN 46556, USA
[d] Science and Safety Policy Research Division, Mitsubishi Research Institute, Inc., 2-3-6 Ōtemachi, Chiyoda-ku, Tokyo 100-8141, Japan

ARTICLE INFO

ABSTRACT

The shallow water equations are used to model large-scale surface flow in the ocean, coastal rivers, estuaries, salt marshes, bays, and channels. They can describe tidal flows as well as storm surges associated with extreme storm events, such as hurricanes. The resulting currents can transport bed load and suspended sediment and result in morphological changes to the seabed. Modeling these processes requires tightly coupling a bed morphology equation to the shallow water equations. Discontinuous Galerkin finite element methods are a natural choice for modeling this coupled system, given the need to solve these problems on unstructured computational meshes, as well as the desire to implement hp-adaptivity for capturing the dynamic features of the solution. However, because of the presence of non-conservative products in the momentum equations, the standard DG method cannot be applied in a straightforward manner. To rectify this situation, we summarize and follow an extended approach described by Rhebergen et al., which uses theoretical results due to Dal Maso et al. appearing in earlier work. In this paper, we focus on aspects of the implementation of the morphological model for bed evolution within the Advanced Circulation (ADCIRC) modeling framework, as well as the verification of the RKDG method in both h (mesh spacing) and p (polynomial order). This morphological model is applied to a number of coastal engineering problems, and numerical results are presented, with attention paid to the effects of h- and p-refinement in these applications. In particular, it is observed that for sediment transport, piecewise constant (i.e., finite volume) approximations of the bed are very over-diffusive and lead to poor sediment solutions.

© 2010 Elsevier B.V. All rights reserved.

1. Introduction

The modeling of flow and transport in coastal waters requires a detailed knowledge of winds, waves, currents, sediment transport and ultimately, the resulting morphological changes in the seabed that occur as a result of these processes. The erosion and deposition of bed sediment can have a major detrimental impact on the coastal population, infrastructure, and environment. For example, the US Army Corps of Engineers (USACE) maintains more than 12,000 miles of waterways for transportation, which carry approximately one-sixth of the US inter-city freight [1]. Maintenance of these waterways through dredging and backfilling operations represents a significant cost to the USACE as well as other agencies and industries. As another example, the structural integrity of bridges, levees,

and piers can be compromised by excessive scour of the seabed around the structure. Also, dune, barrier island, and channel erosion during a hurricane leads to the removal of major flow controls, which significantly affects inland inundation. In addition to these infrastructure-related issues, there exists a host of environmental concerns, such as beach erosion and the transport of contaminants with sediment, which may actually act as a source or sink for contaminants depending on the surrounding physico-chemical conditions [2].

Collectively, the various fluid flow and transport processes that lead to morphological changes in the seabed form an interdependent physical system in which the fluid motion, due to both waves and currents, drives the transport of sediment, which dictates the morphological evolution of the seabed. In turn, the fluid motion itself is then directly affected by the morphological changes in the bed that it induces. Comprehensive modeling of these processes in the coastal zone presents several challenges and open questions. Most existing hydrodynamic models use a fixed-bed approach; that is, the bottom boundary of the seabed is not allowed to evolve

in response to the fluid motion. With respect to movable-bed models, there is no single, generally accepted mathematical model that is used, with descriptions of the fluid-bed interface region varying from simple single interface models to more complex three-phase approaches that consist of fluid, fluid-sediment, and sediment phases; see, for example, [3]. Once an appropriate mathematical model is formulated, there exists the numerical challenge of coupling models of various processes that exhibit disparate time scales—both within the fluid motion itself and between the fluid and bed motion. The evolution of the bed is typically on a much slower time scale compared to even the slowest time scale of the fluid motion; a situation where this may not be the case is during an extreme event, such as a hurricane.

In this paper, we focus on the coupling of shallow water hydrodynamics with sediment transport described as bed load, and the application of an *hp* Runge–Kutta discontinuous Galerkin (RKDG) approximation to this coupled system. The mathematical model we consider consists of the depth-averaged (two-dimensional) shallow water equations and the well-known Exner equation [4], which describes the bed morphology. The models are coupled in the sense that the sediment flux depends on the current, while the transport of sediment induces dynamic bathymetry, which affects the water depth. In addition, the fact that bathymetry is now an unknown in the model rather than a known fixed quantity gives rise to a non-conservative product in the shallow water momentum equations, which requires special treatment.

The RKDG method is an extension of finite volume methods which allows for arbitrary order of approximation in space and is applicable to general unstructured meshes. A number of researchers have studied finite volume methods for circulation/sediment transport/bed morphology models of various levels of complexity, in one and two space dimensions; see for example [3,5–12]. These papers shed light on approaches for coupling the equations in both space and time, including the development of numerical fluxes appropriate for DG discretizations.

Recently, Tassi et al. [13] have examined river bed evolution in shallow water flow using the RKDG method. The DG spatial discretization that is used is an extended approach developed by Rhebergen et al. [14] to handle the non-conservative product that is introduced when coupling the Exner equation to the shallow water equations. We follow this approach here, but focus on the verification of the RKDG method in both *h* (mesh spacing) and *p* (polynomial order), and on the application of the model to a number of coastal engineering problems, again emphasizing the effects of *h*- and *p*-refinement in these examples.

The work described herein is the latest in a series of papers by the authors and collaborators on the application of discontinuous Galerkin (DG) methods to shallow water flows [15–22]. The RKDG method has been implemented within the general Advanced Circulation (ADCIRC) modeling framework, which is a parallel simulator for shallow water flow and transport coupled with wind, wind-waves and other external forcings. The operational ADCIRC model, which is based on a continuous Galerkin method applied to the so-called Generalized Wave Continuity Equation (GWCE), has been used to study a variety of coastal engineering applications, including storm surges generated by hurricanes and tropical storms [23,24]. The coupling of the GWCE-based formulation with a DG method for bed morphology has been studied by the authors in [25]; however, this coupling suffers from the fact that the GWCE method does not produce locally conservative currents, which can lead to spurious sediment transport solutions. One of the immediate goals of our research is the development of a DG-based hydrodynamic storm surge model coupled to sediment transport, for modeling scour due to strong currents during extreme storm events.

The remainder of this paper is outlined as follows. In Section 2 we present the governing equations for hydrodynamics and bed morphology. As mentioned above, the presence of dynamic bathymetry gives rise to a non-conservative product in the formulation. The analysis of such models is due to Dal Maso et al. [26], and we summarize their theoretical results. This formulation is the basis of the RKDG method as originally presented by Rhebergen et al. [14]. This formulation is described in Section 3 along with some details of the implementation. In Section 4, several numerical studies are presented. These studies begin by highlighting the convergence of the method in both *h* and *p* for a problem with an analytical solution. We then focus on a number of coastal engineering applications, including flow through a converging channel, scouring around a bridge pier, and ebb and flood shoal formation in an inlet. In each application, we study the effects of *h*- and/or *p*-refinement within the RKDG formulation. We conclude in Section 4.5 with some remarks on parallel performance.

2. Model description

2.1. Governing equations

The governing equations for hydrodynamics are derived by integrating the Navier–Stokes equations with kinematic boundary conditions over depth, assuming a hydrostatic pressure distribution as well as a uniform velocity profile in the vertical, and ignoring the effects of diffusion. The following system of equations are obtained:

$$\partial_t H + \nabla \cdot \mathbf{q} = 0, \tag{1a}$$
$$\partial_t \mathbf{q} + \nabla \cdot \mathbf{F}_{\text{mom}} - gH\nabla b = \mathbf{s}_{\text{mom}}, \tag{1b}$$

which, taken together, are known as the Saint–Venant or shallow water equations (SWE), which are defined on the domain $\Omega \times (0,T]$ with appropriate initial and boundary conditions specified.

In (1a) and (1b), $H = \zeta + b$ is the total depth of the seawater column, where ζ is the observed free surface elevation measured positive upward from a specified horizontal datum and b is the bathymetric depth measured positive downward from the datum, as shown in Fig. 1. The vector $\mathbf{q} = (Hu, Hv)^T$ is the discharge rate, where u and v are the depth-averaged velocities in the *x*- and *y*-directions, respectively. The symmetric tensor

$$\mathbf{F}_{\text{mom}} = \begin{pmatrix} Hu^2 + \frac{1}{2}gH^2 & Huv \\ Huv & Hv^2 + \frac{1}{2}gH^2 \end{pmatrix},$$

where the constant $g = 9.80665$ m/s² is standard gravity, and $\mathbf{s}_{\text{mom}}$ represents terms such as bottom friction, turbulent eddy viscosity, and additional surface forces from the Coriolis force and tide-generating potential as well as surface stresses caused by wind, variable atmospheric pressure, and radiation stresses from short wind-driven waves. Note that H and $\mathbf{q}$ are both functions of time *t* as well as space.
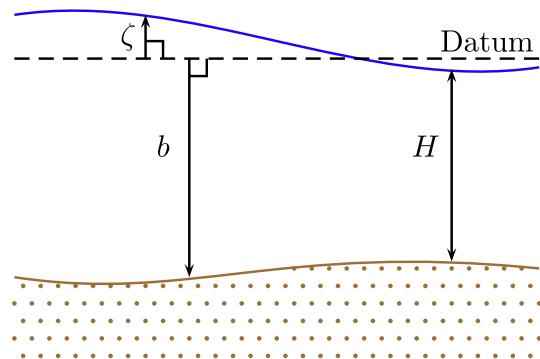

Fig. 1. The seawater column, showing the relationship between H, ζ, and b.

In addition, sediment mass balance within the water column is considered. Under the assumptions of constant porosity ε_0 and ignoring the effects of diffusion, the following sediment transport equation arises:

$$\frac{\partial b}{\partial t} - \frac{1}{1 - \varepsilon_0} \nabla \cdot \mathbf{q}_b = 0, \tag{2}$$

where $\mathbf{q}_b$ is the total sediment transport rate. This is an empirically defined function of H, $\|\mathbf{u}\|_2 = \sqrt{u^2 + v^2}$, and several other variables; see, for example, [27]. In the numerical results presented in this paper, only bed load transport due to currents is considered, and $\mathbf{q}_b$ is a taken as a function of $\|\mathbf{u}\|_2^3$ except where otherwise noted.

For the purposes of this paper, the coupled system consisting of Eqs. (1a), (1b), and (2) will be expressed as

$$\partial_t \mathbf{w} + \nabla \cdot \mathbf{F} + \mathcal{G} \nabla \mathbf{w} - \mathbf{s} = \mathbf{0}, \tag{3}$$

where $\mathbf{w} = (H, Hu, Hv, b)^T$, $\mathbf{F} = (\mathbf{q} \mid \mathbf{F}_{\text{mom}} \mid \mathbf{q}_b)^T$, $\mathcal{G} \nabla \mathbf{w} = (0, -gH\partial_x b, -gH\partial_y b, 0)^T$ where $\mathcal{G}$ is a third-order tensor, and $\mathbf{s} = (0, \mathbf{s}_{\text{mom}}^T, 0)^T$.

2.2. Treatment of discontinuous bathymetry

In its present form, the coupled system (3) presents several challenges when attempting to resolve all components of $\mathbf{w}$ simultaneously. This is partly rooted in the fact that transport of sediment is a non-passive quantity; two-way coupling results since changes in bathymetry directly affect both the elevation and flow rate and vice versa. The more serious issue, however, is the presence of the non-conservative products $-gH\partial_x b$ and $-gH\partial_y b$ in the momentum Eq. (1b). Since the quantity $-gH$ cannot be expressed as the Jacobian of some tensor $\mathbf{Q}$, the hyperbolic system (3) cannot be written in so-called divergence form:

$$\partial_t \mathbf{w} + \nabla \cdot \mathbf{Q} = \mathbf{0}. \tag{4}$$

The problem becomes particularly acute when b is discontinuous, which frequently occurs in many ocean, riverine, and estuarine systems. This is because weak solutions to (3) do not exist in this case; the distributional derivatives are not defined at the discontinuities [14]. As a result, traditional discontinuous Galerkin (DG) methods cannot be applied to this system in a straightforward manner.

There are three options available to treat this shortcoming. The first is to use the fully non-conservative form of (3). Indeed, by considering the fully non-conservative form of the coupled system in one space dimension, adjusted characteristic speeds may be extracted and incorporated into the definition of, for example, the Local Lax–Friedrichs (LLF) numerical flux, and the system may then be expressed in divergence form. However, in two space dimensions, this approach fails. Moreover, this option is not very attractive from a numerical point of view, since the numerical method may then possibly converge to non-physical (i.e. non-entropy-preserving) solutions [16].

The second choice involves uncoupling the sediment transport Eq. (2) from the SWE (1a) and (1b), at least to some degree. Based on physical arguments involving typical time scales for sediment and seawater transport rates, this approach was previously taken in our model implementation [16]. The principal drawback to this approach is its lack of accuracy during instances when the time scales for transport of sediment and seawater become similar, such as during the extreme events ultimately desired to simulate.

The remaining option is to formulate a special treatment for the non-conservative products. This was done in previous work for one-dimensional problems in [28] and for two-phase flow problems in [29]. An alternative treatment was proposed by Dal Maso et al. [26] and applied by Rhebergen et al. to one- and two-dimensional problems using the DG method with piecewise linear finite element basis functions in [14]. It is this treatment that will be employed here.

The idea proposed by Dal Maso et al. is to regularize the solution $\mathbf{w}$ near discontinuities by connecting the interior and exterior traces $\mathbf{w}^{(\text{in})}$ and $\mathbf{w}^{(\text{ex})}$ (assuming these are well-defined) with a smooth path function $\phi : [0, 1] \to \mathbb{R}^4$ parameterized by $\tau \in [0, 1]$. This path ϕ must satisfy the following properties:

1. [End conditions] $\phi(0) = \mathbf{w}^{(\text{in})}$ and $\phi(1) = \mathbf{w}^{(\text{ex})}$,
2. [Consistency] If $\mathbf{w}^{(\text{in})} = \mathbf{w}^{(\text{ex})}$, then $\phi(\tau) = \mathbf{w}^{(\text{in})}$,

3. [Lipschitz] For each component ϕ_k of ϕ, $\exists M > 0$ such that

$$\left| \frac{\partial \phi_k}{\partial \tau} \right| \leqslant M \left| w_k^{(\text{in})} - w_k^{(\text{ex})} \right|$$

for a.e. $\tau \in [0, 1]$, and
4. [Symmetry] In two or more space dimensions,

$$\phi(\tau; \mathbf{w}^{(\text{in})}, \mathbf{w}^{(\text{ex})}) = \phi(1 - \tau; \mathbf{w}^{(\text{ex})}, \mathbf{w}^{(\text{in})}).$$

Condition (4) states that the path must be symmetric with respect to an interchange of the traces. This condition need not be satisfied for one-dimensional problems [14,26].

Defining the third-order tensor $\mathcal{T}$ as

$$\mathcal{T} = \partial_{\mathbf{w}} \mathbf{F} + \mathcal{G}, \tag{5}$$

Eq. (3) may be rewritten as

$$\partial_t \mathbf{w} + \mathcal{T} \nabla \mathbf{w} - \mathbf{s} = \mathbf{0}. \tag{6}$$

With the coupled system expressed by (6) in this non-conservative form, we may state the following theorem, due to Dal Maso et al. [26], on the integration of non-conservative products, which are treated as a bounded Borel measure:

Theorem 1. *Assume that*

1. *The function $\mathbf{w}$ is bounded on its domain Ω,*
2. *The function $\mathbf{w}$ is of bounded variation on Ω,*
3. *Each entry of $\mathcal{T}$ is a locally bounded, measurable function that maps Borel sets to Borel sets, and*
4. *The domain $\Omega = \Omega^C \cup \Omega^J \cup \Omega^I$ with each subset disjoint, where Ω^C is the set where $\mathbf{w}$ is almost everywhere continuous, Ω^J is the set of jumps in $\mathbf{w}$, and Ω^I is the set of "irregular" points (an example of which is given in Section 3.1).*

Then there exists a unique, bounded vector of Borel measures $\boldsymbol{\mu} : \Omega \to \mathbb{R}^4$ such that

1. *If B is a Borel subset of Ω^C, then*

$$\boldsymbol{\mu}(B) = \int_B \mathcal{T} \nabla \mathbf{w} \, d\lambda,$$

where λ is the Borel measure,
2. *If B is a Borel subset of Ω^J, then*

$$\boldsymbol{\mu}(B) = \int_{B \cap \Omega^J} \left(\int_0^1 \mathcal{T}(\phi) \frac{\partial \phi}{\partial \tau} \, d\tau \right) \mathbf{n} \, dH^2,$$

where $\mathbf{n}$ is the unit vector normal to B directed toward the region where $\tau = 1$ (where $\mathbf{w} = \mathbf{w}^{(\text{ex})}$), H^2 is the two-dimensional Hausdorff measure, and
3. *If B is a Borel subset of Ω^I, then*

$$\boldsymbol{\mu}(B) = \mathbf{0}.$$

Consult [26] for the proof. The second assumption is necessary since it guarantees that $\mathbf{w}^{(\text{in})}$ and $\mathbf{w}^{(\text{ex})}$ are well-defined, and also ensures that $\mathbf{w}$ admits only jump-type discontinuities on Ω.

3. Finite element discretization

3.1. DG formulation

In this section, we derive the DG formulation of (6). We begin by defining appropriate finite element function spaces to be used in the model. Next, we construct an unstructured finite element mesh or grid from Ω. Then we apply Theorem 1 to integrate the non-conservative product in (6) over the mesh. Finally, we describe the numerical flux to be used on element boundaries.

Let $\Omega_h = \cup_e \Omega_e$ be a finite element partition of Ω into a set of non-overlapping triangular elements Ω_e. The solution $\mathbf{w}$ is approximated in Ω_h by $\mathbf{w}_h$ residing in the finite element space

$$W_h = [L_\infty(0,T;V_h)]^4,$$

where

$$V_h = \{v \in BV(\Omega_h) : v|_{\Omega_e} \in \mathcal{P}^p(\Omega_e) \; \forall \Omega_e \in \Omega_h\},$$

where $BV(\Omega_h)$ denotes the space of functions of bounded variation on Ω_h (required for Theorem 1), and $\mathcal{P}^p(\Omega_e)$ denotes the space of polynomials of order p on the element Ω_e. In this paper, we assume p is constant over the domain; see [16,20] for commentary on implementing p-adaptivity.

The semi-discrete weak formulation of the coupled system is derived following the approach discussed in [13,14]. Multiplying Eq. (6) by a test function $\mathbf{v}_h \in W_h$ and integrating over Ω_h gives

$$(\partial_t \mathbf{w}_h, \mathbf{v}_h)_{L_2(\Omega_h)} + \int_{\Omega_h} \mathbf{v}_h \cdot d\boldsymbol{\mu} - (\mathbf{s}_h, \mathbf{v}_h)_{L_2(\Omega_h)} = 0, \tag{7}$$

where Theorem 1 implies that

$$d\boldsymbol{\mu} = \begin{cases} \mathcal{T}_h \nabla \mathbf{w}_h d\Omega_h^C & \text{on } \Omega_h^C, \\ \left(\int_0^1 \mathcal{T}_h(\boldsymbol{\phi})\frac{\partial \boldsymbol{\phi}}{\partial \tau} d\tau\right)\mathbf{n} d\Omega_h^J & \text{on } \Omega_h^J, \\ \mathbf{0} & \text{on } \Omega_h^I. \end{cases} \tag{8}$$

In this context, Ω_h^C represents the interiors of all elements Ω_e; Ω_h^J, the set of all element boundaries $\partial\Omega_e$; Ω_h^I, the set of all nodal points—a set of Borel measure zero.

With $d\boldsymbol{\mu}$ defined by Eq. (8), Eq. (7) becomes

$$0 = \sum_e (\partial_t \mathbf{w}_h + \mathcal{T}_h \nabla \mathbf{w}_h - \mathbf{s}_h, \mathbf{v}_h)_{L_2(\Omega_e)}$$
$$+ \sum_{e_I} \left\langle \left(\int_0^1 \mathcal{T}_h(\boldsymbol{\phi})\frac{\partial \boldsymbol{\phi}}{\partial \tau} d\tau\right)\mathbf{n}, \mathbf{v}_h \right\rangle_{L_2(\gamma_{e_I})},$$

where the terms are now written element-wise, and γ_{e_I} denotes an interior edge. Splitting $\mathcal{T}_h$ using Eq. (5) results in

$$0 = \sum_e (\partial_t \mathbf{w}_h + \nabla \cdot \mathbf{F}_h + \mathcal{G}_h \nabla \mathbf{w}_h - \mathbf{s}_h, \mathbf{v}_h)_{L_2(\Omega_e)}$$
$$+ \sum_{e_I} \left\langle \left(\int_0^1 \mathcal{G}_h(\boldsymbol{\phi})\frac{\partial \boldsymbol{\phi}}{\partial \tau} d\tau\right)\mathbf{n}, \mathbf{v}_h \right\rangle_{L_2(\gamma_{e_I})}. \tag{9}$$

Since the test function $\mathbf{v}_h$ is double-valued on element boundaries, an appropriate numerical flux $\hat{\mathbf{v}}_h$ must be chosen. This numerical flux is chosen in [14] such that the DG formulation with non-conservative products reduces to the conservative DG formulation whenever $\mathcal{G}_h$ is the Jacobian of some tensor $\mathbf{Q}_h$. To this end, Rhebergen et al. [14] prove that

$$\hat{\mathbf{v}}_h = \{\{\mathbf{v}_h\}\} = \frac{\mathbf{v}_h^{(in)} + \mathbf{v}_h^{(ex)}}{2}$$

satisfies this requirement. Thus, $\mathbf{v}_h$ may be replaced with $\{\{\mathbf{v}_h\}\}$ in the boundary integrals of Eq. (9), and the divergence term in the element interior integral may be integrated by parts to obtain

$$0 = \sum_e (\partial_t \mathbf{w}_h + \mathcal{G}_h \nabla \mathbf{w}_h - \mathbf{s}_h, \mathbf{v}_h)_{L_2(\Omega_e)} - \sum_e (\mathbf{F}_h, \nabla \mathbf{v}_h)_{L_2(\Omega_e)}$$
$$+ \sum_{e_I} \left\langle \hat{\mathbf{f}}_{nc}, [\![\mathbf{v}_h]\!] \right\rangle_{L_2(\gamma_{e_I})} + \sum_{e_I} \left\langle \left(\int_0^1 \mathcal{G}_h(\boldsymbol{\phi})\frac{\partial \boldsymbol{\phi}}{\partial \tau} d\tau\right)\mathbf{n}, \{\{\mathbf{v}_h\}\} \right\rangle_{L_2(\gamma_{e_I})}$$
$$+ \sum_{e_B} \left\langle \hat{\mathbf{f}}_{nc}, \mathbf{v}_h^{(in)} \right\rangle_{L_2(\gamma_{e_B})}, \tag{10}$$

where γ_{e_B} represents a boundary edge, $[\![\cdot]\!] = (\cdot)^{(in)} - (\cdot)^{(ex)}$ represents the so-called jump operator, and $\hat{\mathbf{f}}_{nc}$ is a numerical flux to be defined later.

The derivation thus far has been independent of the exact form of the path $\boldsymbol{\phi}$. However, with $\mathbf{w}_h$ regularized near the element boundaries in this manner, the value of the regularized non-conservative product, and hence the value of the path integral, is ultimately dependent in the limit on the choice of path (see, for example, [14] or [26]). As a consequence, Eq. (10) cannot be further simplified until a suitable form of $\boldsymbol{\phi}$ is chosen. Rhebergen et al. in [14] investigated the effect on numerical solutions for polynomial paths of various orders, as well as those chosen by Toumi in [30]. They found that the effect on the numerical solution is small, and that having a good numerical integration scheme to integrate the path integral appears to be of greater importance [14]. With this result in mind, a linear path will be used in the implementation and in all results presented in this paper:

$$\boldsymbol{\phi}(\tau) = \mathbf{w}_h^{(in)} + \tau\left(\mathbf{w}_h^{(ex)} - \mathbf{w}_h^{(in)}\right).$$

This choice of path allows for easy evaluation of the path integral: Define

$$\mathbf{v}_{nc} = \left(\int_0^1 \mathcal{G}_h(\boldsymbol{\phi})\frac{\partial \boldsymbol{\phi}}{\partial \tau} d\tau\right)\mathbf{n} = \begin{pmatrix} 0 \\ g\{\{H_h\}\}[\![b_h]\!]n_x \\ g\{\{H_h\}\}[\![b_h]\!]n_y \\ 0 \end{pmatrix}.$$

Eq. (10) can then be rewritten as

$$0 = \sum_e (\partial_t \mathbf{w}_h + \mathcal{G}_h \nabla \mathbf{w}_h - \mathbf{s}_h, \mathbf{v}_h)_{L_2(\Omega_e)} - \sum_e (\mathbf{F}_h, \nabla \mathbf{v}_h)_{L_2(\Omega_e)}$$
$$+ \sum_{e_I} \left\{ \left\langle \hat{\mathbf{f}}_{nc}, [\![\mathbf{v}_h]\!] \right\rangle_{L_2(\gamma_{e_I})} + \left\langle \mathbf{v}_{nc}, \{\{\mathbf{v}_h\}\} \right\rangle_{L_2(\gamma_{e_I})} \right\}$$
$$+ \sum_{e_B} \left\langle \hat{\mathbf{f}}_{nc}, \mathbf{v}_h^{(in)} \right\rangle_{L_2(\gamma_{e_B})}.$$

To finalize the derivation, it remains to define an appropriate (stable) numerical flux and merge the boundary integrals. As discussed in [14], the form of this flux may be thought of as a sum of an average term of $\mathbf{F}_h$, a stabilizing viscous term involving $[\![\mathbf{w}_h]\!]$, and an additional stabilizing term involving $\mathbf{v}_{nc}$, the value of the path integral. We define

$$\hat{\mathbf{f}}_{nc} = \left(\hat{\mathbf{f}}_{nc,hydro}^T, \hat{f}_{nc,sed}\right)^T,$$

where the numerical flux for the hydrodynamic part of the system (Eqs. (1a) and (1b)) is defined, following [14], as

$$\hat{\mathbf{f}}_{nc,hydro} = \begin{cases} \mathbf{F}_h^{(in)}\mathbf{n} - \frac{1}{2}\mathbf{v}_{nc} & S^{(in)} > 0, \\ \hat{\mathbf{f}}^{HLL} - \frac{S^{(in)}+S^{(ex)}}{2(S^{(ex)}-S^{(in)})}\mathbf{v}_{nc} & S^{(in)} < 0 < S^{(ex)}, \\ \mathbf{F}_h^{(ex)}\mathbf{n} + \frac{1}{2}\mathbf{v}_{nc} & S^{(ex)} < 0, \end{cases} \tag{11}$$

where

$$S^{(in)} = \min\left\{\mathbf{u}_h^{(in)} \cdot \mathbf{n} - \sqrt{gH_h^{(in)}}, \mathbf{u}_h^{(ex)} \cdot \mathbf{n} - \sqrt{gH_h^{(ex)}}\right\},$$

$$S^{(ex)} = \max\left\{\mathbf{u}_h^{(in)} \cdot \mathbf{n} + \sqrt{gH_h^{(in)}}, \mathbf{u}_h^{(ex)} \cdot \mathbf{n} + \sqrt{gH_h^{(ex)}}\right\}$$

are the truncated characteristic speeds (found by considering the eigenvalues of the hydrodynamic part of $\mathcal{T}$), and

$$\hat{\mathbf{f}}^{\text{HLL}} = \frac{\left(S^{(\text{ex})}\mathbf{F}_h^{(\text{in})} - S^{(\text{in})}\mathbf{F}_h^{(\text{ex})}\right)\mathbf{n}}{S^{(\text{ex})} - S^{(\text{in})}} - \frac{S^{(\text{in})}S^{(\text{ex})}[\![\mathbf{w}_h]\!]}{S^{(\text{ex})} - S^{(\text{in})}}$$

is the Harten–Lax–van Leer (HLL) flux defined in [31]. It should be noted that for most problems in shallow water hydrodynamics, the Froude number rarely exceeds 0.2, and therefore only the second case of Eq. (11) is frequently encountered [32].

For the sediment transport Eq. (2), an upwind flux is used, based upon the assumption that transport is always in the direction of the flow. This choice of numerical flux is known to work well in practice [16]. It is defined as

$$\hat{f}_{\text{nc,sed}} = \begin{cases} \mathbf{q}_{b,h}^{(\text{in})} \cdot \mathbf{n} & \mathbf{u}_h^{\text{Roe}} \cdot \mathbf{n} \geqslant 0, \\ \mathbf{q}_{b,h}^{(\text{ex})} \cdot \mathbf{n} & \mathbf{u}_h^{\text{Roe}} \cdot \mathbf{n} < 0, \end{cases}$$

where

$$\mathbf{u}_h^{\text{Roe}} = \frac{\mathbf{u}_h^{(\text{in})}\sqrt{H_h^{(\text{in})}} + \mathbf{u}_h^{(\text{ex})}\sqrt{H_h^{(\text{ex})}}}{\sqrt{H_h^{(\text{in})}} + \sqrt{H_h^{(\text{ex})}}}$$

is the so-called Roe-averaged value of the velocity $\mathbf{u}_h$.

By introducing ghost values for $\mathbf{w}^{(\text{ex})}{}_h$, $\mathbf{v}^{(\text{ex})}{}_h$, etc. on the domain boundary, the interior and boundary edge integrals may be combined because the expression for the numerical flux $\hat{\mathbf{f}}_{\text{nc}}$ is the same. Therefore, the final form of the DG finite element discretization is

$$0 = \sum_e \left(\partial_t\mathbf{w}_h + \mathcal{G}_h\nabla\mathbf{w}_h - \mathbf{s}_h, \mathbf{v}_h\right)_{L_2(\Omega_e)} - \sum_e \left(\mathbf{F}_h, \nabla\mathbf{v}_h\right)_{L_2(\Omega_e)}$$
$$+ \sum_e \left\{\left\langle\hat{\mathbf{f}}_{\text{nc}}, [\![\mathbf{v}_h]\!]\right\rangle_{L_2(\partial\Omega_e)} + \left\langle\mathbf{v}_{\text{nc}}, \{\!\{\mathbf{w}_h\}\!\}\right\rangle_{L_2(\partial\Omega_e)}\right\}. \tag{12}$$

3.2. Implementation overview

In this section, a brief summary of our numerical model will be given, including some details about the choice of basis functions and the time stepping scheme used. For a more complete description pertaining to the current implementation of these items, consult [16] or [18].

Recall from Section 3.1 that each element Ω_e is assumed to be triangular. This choice of element allows for greater flexibility when handling unstructured meshes, such as those used in the numerical examples described in Section 4. On each element Ω_e, the DG solution $\mathbf{w}_h$ and test function $\mathbf{v}_h$ may be expanded as

$$\mathbf{w}_h(t,x,y)|_{\Omega_e} = \sum_{l=1}^N \mathbf{w}_{h,l,e}(t)\phi_l(x,y), \tag{13}$$

$$\mathbf{v}_h(t,x,y)|_{\Omega_e} = \sum_{m=1}^N \mathbf{v}_{h,m,e}(t)\phi_m(x,y), \tag{14}$$

where $\{\mathbf{w}_{h,l,e}(t)\}_{l=1}^N$ and $\{\mathbf{v}_{h,m,e}(t)\}_{m=1}^N$ are the sets of local degrees of freedom,

$$N = \frac{(p+1)(p+2)}{2}$$

is the number of degrees of freedom on each element, and $\{\phi_l(x,y)\}_{l=1}^N$ is the set of basis functions on the physical element, defined in terms of the basis functions on the master element $\{\hat{\phi}_l(\xi_1,\xi_2)\}_{l=1}^N$ through an affine mapping $G_e : \widehat{\Omega}_e \to \Omega_e$ as

$$\phi_l(x,y) = \hat{\phi}_l\left(G_e^{-1}(x,y)\right),$$

where $\widehat{\Omega}_e$ is the master triangular element defined by

$$\widehat{\Omega}_e = \{(\xi_1,\xi_2) \in \mathbb{R}^2 : \xi_1 > -1, \ \xi_2 > -1, \ \xi_1 + \xi_2 < 0\}.$$

Substituting the expansions (13) and (14) into Eq. (12) yields an algebraic linear system of ordinary differential equations

$$\sum_e \mathbf{M}_e \frac{d\mathbf{W}_{h,e}}{dt} = \sum_e \mathbf{R}_{h,e}, \tag{15}$$

where $\mathbf{M}_e$ is the $N \times N$ elemental mass matrix defined as

$$[M_e]_{lm} = \int_{\Omega_e} \phi_l(x,y)\phi_m(x,y)d\Omega_e,$$

the $N \times 4$ matrix $\mathbf{W}_{h,e}$ contains the degrees of freedom, and the $N \times 4$ matrix $\mathbf{R}_{h,e}$ denotes the remaining terms on the right-hand side of Eq. (12).

In order to solve the system (15) for $\mathbf{W}_{h,e}$, we invert $\mathbf{M}_e$, and then apply a time stepping scheme. Using an $L_2(\widehat{\Omega}_e)$-orthogonal basis reduces the mass matrix $\mathbf{M}_e$ to a diagonal one, which may be trivially inverted. For this reason, a hierarchical basis with the $L_2(\widehat{\Omega}_e)$-orthogonality property proposed by Dubiner in [33] has been implemented.

The time stepping scheme utilized is an explicit strong-stability preserving (SSP) s-stage, kth-order Runge–Kutta scheme, where the pair (s,k) is one of $(1,1)$, $(s,2)$ with $s \geqslant 2$, $(s,3)$ with $3 \leqslant s \leqslant 8$, or $(s,4)$ with $5 \leqslant s \leqslant 8$. The SSP RK scheme is designed so that if the forward Euler method is stable under a given semi-norm and Courant–Friedrichs–Lewy (CFL) condition, then the higher-order scheme remains stable under the same semi-norm, but perhaps a different CFL condition [16]. These methods also possess the desirable total-variation-diminishing (TVD) property. This time stepping method takes the following general form:

Algorithm 1 (*SSP RK scheme*). For each time step from t_n to t_{n+1},

1. Set $\mathbf{W}_{h,e}^{(0)} \leftarrow \mathbf{W}_{h,e}(t_n)$.
2. For each stage $i = 1, 2, \ldots, s$, set

$$\mathbf{W}_{h,e}^{(i)} \leftarrow \sum_{j=1}^i \left\{\alpha_{ij}\mathbf{W}_{h,e}^{(j-1)} + \beta_{ij}\Delta t\mathbf{M}_e^{-1}\mathbf{R}_{h,e}\left(\mathbf{W}_{h,e}^{(j-1)}, t_n + \delta_j\Delta t\right)\right\}.$$

3. Set $\mathbf{W}_{h,e}(t_{n+1}) \leftarrow \mathbf{W}_{h,e}^{(s)}$.

In the algorithm above, $\delta_j = \sum_{k=1}^{j-1}\gamma_{j-1,k}$ is a vector of length s of time-lagging parameters, and the $s \times s$ matrices $\boldsymbol{\alpha}$, $\boldsymbol{\beta}$, and $\boldsymbol{\gamma}$ are optimized parameters with respect to maximization of the CFL number. They satisfy the TVD constraints

$$\alpha_{ij} \geqslant 0,$$

$$\sum_{j=1}^i \alpha_{ij} = 1, \quad \text{and}$$

$$\gamma_{ij} = \beta_{ij} + \sum_{k=j}^{i-1}\gamma_{kj}\alpha_{i,k+1}.$$

To be clear, it should be noted that Algorithm 1 must be performed for each degree of freedom on every element Ω_e. Refer to [16,18,34] for further details on SSP RK methods, and to [20] for values of $\boldsymbol{\alpha}$ and $\boldsymbol{\beta}$.

We conclude this section with some remarks on the use of slope limiting. To eliminate local overshoots and undershoots, four different choices of slope limiters are implemented as post-processing routines for $\mathbf{W}_{h,e}(t_{n+1})$. However, we only employ two of these here, since the others are notorious for degrading the solution to first-order accuracy at local extrema (effectively $p = 0$ in these regions), and we wish to test our model with $p > 1$ in the examples listed in Section 4. Thus, when $p = 1$, the limiting procedure formulated by Cockburn and Shu in [35] is used if needed. This is the case for the entire morphodynamic system in Section 4.3, and for the sediment transport equation in Section 4.4. But for $p > 1$, it becomes necessary to make use of a higher-order slope

limiting procedure. For this paper, we implement the algorithm outlined in the work by Xu et al. in [36], which is a local limiting procedure based on the application of a WENO-type limiter to the coefficients of the higher-order Taylor expansion about the element barycenter. It has been shown to work well in practice [36]. For the sake of brevity, we shall not expound upon the implementation details here, but instead we refer the interested reader to Sections 2.1, 2.2, 2.3, and 2.5 of [36]. In this paper, we found that it was only necessary to apply the procedure of Xu et al. to the sediment transport equation for the test cases in Sections 4.2 and 4.4, and to the entire system for the case described in Section 4.3. For the remaining test cases, we found that no limiting was necessary in order to preserve numerical stability.

4. Numerical examples and results

In this section, numerical examples and results using our model are presented. This method is applied to four problems: an evolving dune, a converging channel, scouring around a bridge pier, and an idealized inlet. These simulations were run in parallel (with the exception of the first test case) on the Institute for Computational Engineering and Science's (ICES) `bevo2` cluster, as well as on the Texas Advanced Computing Center's `lonestar` cluster [37].

4.1. Convergence study: evolution of a dune

In this test case, a problem posed by Exner [4] in 1925 is examined. This problem considers the evolution of an initially symmetric mound, or dune, which is subjected to steady, unidirectional flow under the assumption of a rigid-lid (which means that ζ is assumed constant in space and time). Solving this problem allows us to test the sediment transport model independently of the hydrodynamics by comparing the numerical solution to a classical one derived in [4] for the purpose of verifying h- and p-convergence rates. It also allows us to verify and expand upon the results presented in [16] for second- and third-order RKDG schemes.

To properly compare the numerical solution to the exact solution, a simpler model must be used. Exner's model uncouples the sediment transport equation from the SWE by specifying a unidirectional flow velocity as

$$u = \frac{q_f}{H} = \frac{q_f}{\zeta + b},$$
$$v = 0,$$

where q_f is the (non-negative) constant flow discharge rate. Note that under the rigid-lid assumption, ζ is now assumed constant throughout the domain $\Omega = (-\lambda/2, \lambda/2)^2$. Also, it is assumed that $\mathbf{q}_b = (A\|\mathbf{u}\|_2^n, 0)^T$, where A is a non-negative constant and $n = 1$. When $\varepsilon_0 = 0$, Eq. (2) reduces to

$$\frac{\partial b}{\partial t} - \frac{\partial}{\partial x}\left(\frac{Aq_f}{\zeta + b}\right) = 0. \tag{16}$$

Let $b(0, x, y) = b_0(x)$ be the initial data, which is assumed to be sufficiently smooth. Then the exact solution derived in [4] is given implicitly by

$$b(t, x, y) = b_0(x - ct), \tag{17a}$$
$$c(b) = \frac{Aq_f}{(\zeta + b)^2}, \tag{17b}$$

where c denotes the speed at which the top of the dune propagates. This is the same as the characteristic speed.

For this problem, the initial condition is given by

$$b_0(x) = A_0 + A_1 \cos\left(\frac{2\pi x}{\lambda}\right), \tag{18}$$

with $A_0 = 2$, $A_1 = -1$, and $\lambda = 20$. Also, we take $\zeta = 0$ and $Aq_f = 1$ in Eq. (17b). As regards the boundary conditions, the solution is assumed periodic in the x-direction over Ω, so that $b(t, -\lambda/2, y) = b(t, \lambda/2, y)$, with no normal flow at $y = \pm\lambda/2$.

Nonlinear hyperbolic conservation laws have the well-known property that solutions typically develop very steep gradients and eventually discontinuities or shocks. This behavior can be seen in this problem when performing a rudimentary characteristic analysis. Eq. (16) may be written as

$$\frac{\partial b}{\partial t} + \frac{\partial f}{\partial x} = 0,$$

with $f = -Aq_f/(\zeta + b)$, and carrying out the partial derivatives gives the non-conservative form

$$\frac{\partial b}{\partial t} + c(b(x))\frac{\partial b}{\partial x} = 0,$$

where $c(b(x)) = \partial f/\partial b$. Then it can be seen that the breaking time when the shock (or sediment bore) forms is given by

$$t_b = -\left[\min_{\xi} \frac{d}{d\xi} c(b_0(\xi))\right]^{-1} = \frac{5\left(5 - \sqrt{7}\right)^3}{4\pi\sqrt{2\sqrt{7} - 4}} \approx 4.5685 \text{ s}.$$

In our study, four meshes denoted h_1 through h_4 are considered. The coarsest mesh h_1 consists of 800 elements, arranged according to Fig. 2(a). The value of h, defined here as the length of an element in the x-direction, is 1 m. Mesh h_2 is a 1:4 refinement of h_1, with $h = 1/2$ m and 3200 elements (see Fig. 2(b)). This process is repeated to generate meshes h_3 and h_4.

The numerical model is then run until the breaking time t_b is reached. The time step size is set small enough so that the spatial errors dominate the overall error. The DG solution b_h is computed using piecewise constant, linear, quadratic, and cubic basis functions ($p = 0, 1, 2$, and 3) with the SSP (1,1), SSP (2,2), SSP (3,3), and SSP (5,4) time stepping schemes, respectively, and the errors are computed by comparing the approximate solution b_h to the exact solution given by Eqs. (17a) and (17b). The h-convergence results using the $L_\infty(\Omega_h)$-norm at $t = 2$ s and $t = 4$ s are shown in Fig. 3(a) and Fig. 4(a), respectively, while the p-convergence results using mesh h_4 and the $L_\infty(\Omega_h)$-norm at $t = 2$ s and $t = 4$ s are shown in Figs. 3(b) and Fig. 4(b), respectively.

At $t = 2$ s, the solution is still smooth, as this time is well before the time of formation of the shock. Thus, the theoretical h-convergence rate of $p + 1$ is very nearly attained, as can clearly be seen in Fig. 3(a) for the $L_\infty(\Omega_h)$-norm. It should be noted that these rates are also attained for the $L_1(\Omega_h)$- and $L_2(\Omega_h)$-norms, though these results are not shown here. For p-convergence, the theoretical exponential rate is attained, and this is shown in Fig. 3(b).

However, for $t = 4$ s, which is much closer to the breaking time t_b, the h-convergence rates are either seriously degraded (for the cases of $p = 0, 2$, and 3) or obliterated (for the case $p = 1$) when the error over the entire domain Ω_h is under consideration. This is shown in Fig. 4(a) for the $L_\infty(\Omega_h)$-norm, and similar results were obtained for the $L_1(\Omega_h)$- and $L_2(\Omega_h)$-norms. In this case, the largest portion of the error has accumulated in the region $\{(x,y): x \in (4,6), y \in (-10, 10)\}$, which corresponds to the region containing the steepest gradients in the solution, and is also the region containing the shock when $t \geqslant t_b$. This issue demonstrates the need for further h-refinement in this region, as the results shown in Fig. 4(a) appear to display pre-asymptotic behavior. However, when accuracy is considered only in the smooth region of the solution, taken here as

$$\Omega_{sm} = \{(x, y) : x \in (-10, 4), y \in (-10, 10)\},$$

it can be seen in Table 1 that nearly full order of convergence is restored for the cases of $p = 0$ and $p = 1$, while the convergence rates for the cases of $p = 2$ and $p = 3$, though not quite optimal, are much
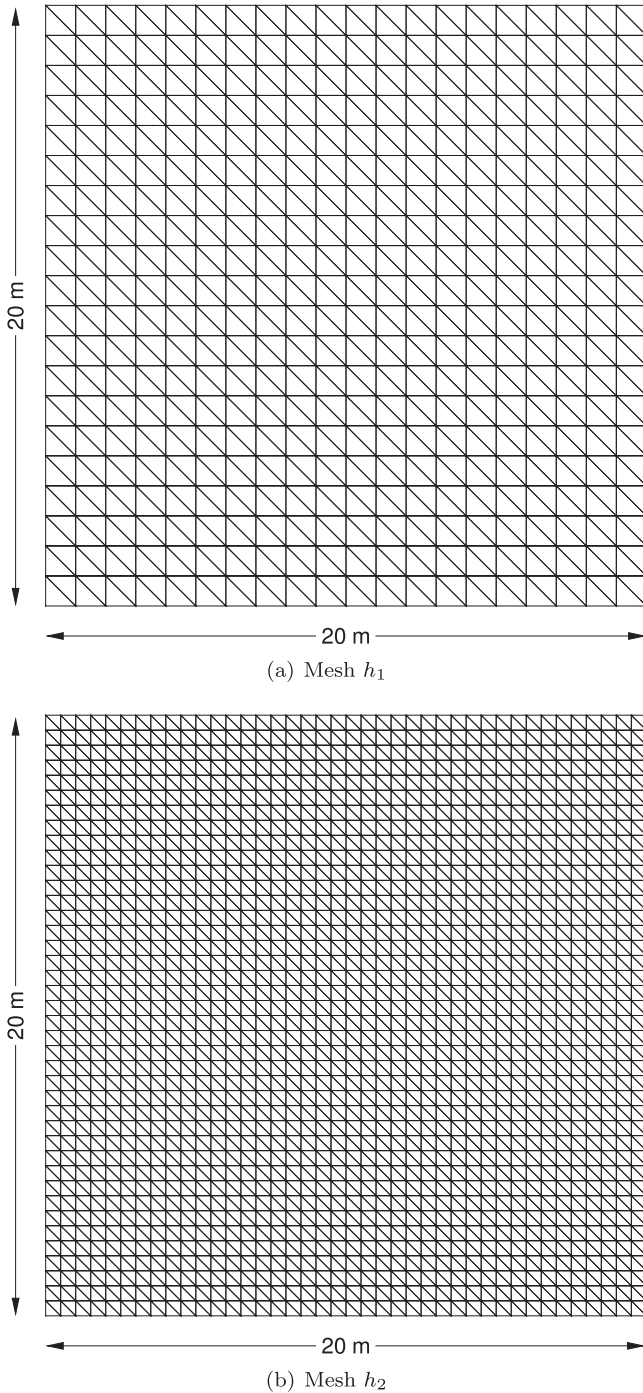
(a) Mesh h_1

(b) Mesh h_2

Fig. 2. Computational meshes (a) h_1 and (b) h_2 showing the h-refinement pattern utilized in the dune evolution test case. Mesh h_3 (not shown) is a 1:4 refinement of mesh h_2, and mesh h_4 (also not shown) is a 1:4 refinement of mesh h_3.
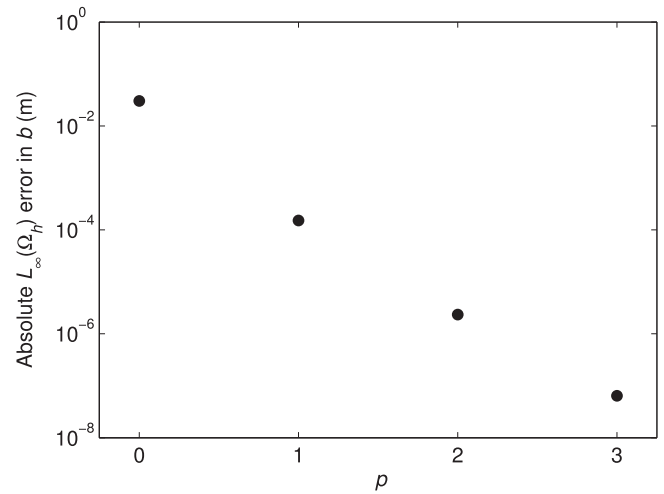

(a) Convergence rates in h
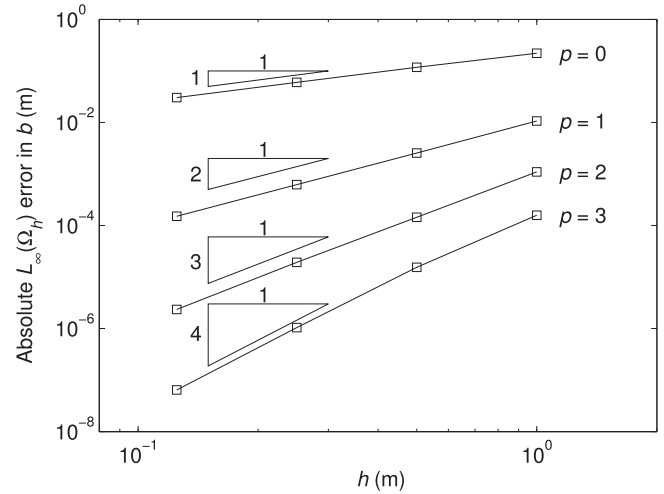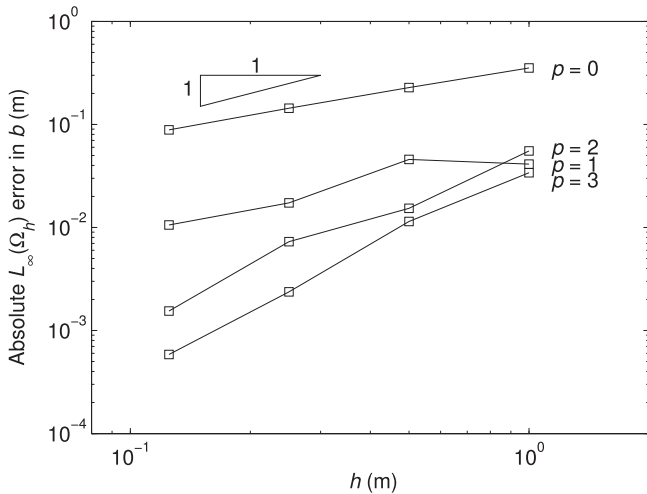

(b) Convergence rates in p

Fig. 3. $L_\infty(\Omega_h)$ convergence rates at $t = 2$ s.

these shortcomings, however, these results show that the model maintains its accuracy in p when h is small enough.
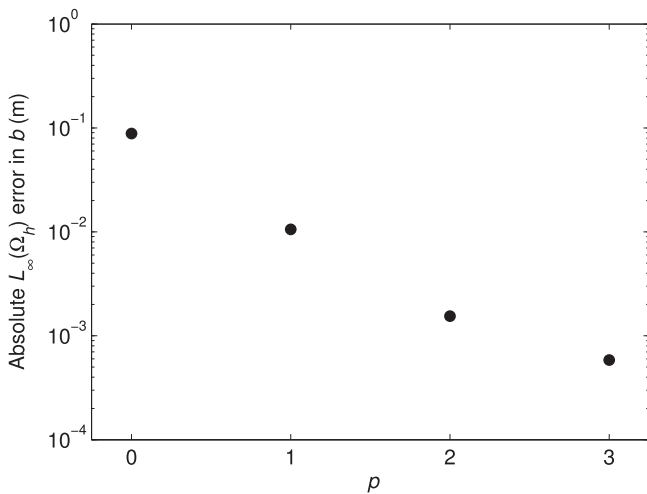
4.2. A converging channel

In [4], Exner extended the model presented for the previous test case to account for channels of varying width with vertical walls. He considered a converging or bottleneck channel with an initially flat bed. This is the computational domain considered in this test case, and it is shown in Fig. 5. The channel considered is 2 km long, 500 m wide at the eastern and western ends, and narrows to a width of 250 m at the center.

Rather than considering the evolution of the bed in a one-dimensional setting, as Exner did, we utilize the full morphological system to consider it in a two-dimensional setting. This allows simultaneously examining both the evolution of the bed and changes in the velocity and flow rate patterns over a 90-day period. For this case, a no normal flow boundary condition is assumed for the northern and southern channel walls, while a fixed inflow rate of 5 m²/s is imposed at the western end of the channel. This rate was chosen so that the flow speed is 0.5 m/s at either end of the channel, with a maximum speed of approximately 1 m/s in the throat of the channel. At the eastern boundary, the elevation is held fixed at $\zeta = 0$, chosen to enforce mass conservation. The bed is ini-

improved, and appear to be tending towards the theoretical rates pending further h-refinement. This verifies that the first- through fourth-order RKDG methods maintain their accuracy and theoretical order of convergence away from the region containing steep gradients and shocks.

In Fig. 4(b), we see that the p-convergence rate at $t = 4$ s does not appear to seriously degrade until $p = 3$. Since the results on mesh h_4 were used here, the effects of the value of h being in the pre-asymptotic regime are mitigated; indeed, the convergence rate is further degraded when using mesh h_3, and no convergence is observed when using meshes h_2 and h_1 (not shown here). Despite

(a) Convergence rates in h

(b) Convergence rates in p

Fig. 4. $L_\infty(\Omega_h)$ convergence rates at $t = 4$ s.

Table 1
Comparison of h-convergence rates at $t = 4$ s on the entire discretized domain Ω_h and on the smooth region Ω_{sm} only.

p	Mesh	L_∞ convergence rates	
		in Ω_h	in Ω_{sm}
0	h_1	...	...
	h_2	0.6305	0.9762
	h_3	0.6641	0.9892
	h_4	0.7001	0.9967
1	h_1	...	...
	h_2	−0.1522	1.8339
	h_3	1.4000	1.7602
	h_4	0.7128	1.8740
2	h_1	...	...
	h_2	1.8513	1.8512
	h_3	1.0743	2.3752
	h_4	2.2383	2.6923
3	h_1	...	...
	h_2	1.5706	3.4398
	h_3	2.2724	3.1037
	h_4	2.0180	3.5808

tially flat, with a bathymetric depth of 10 m. The bottom is also non-porous ($\varepsilon_0 = 0$), and the sediment density is taken as $\rho_s = 2000$ kg/m³, while the median grain size is $d_{50} = 0.2$ mm. For

(a) Coarse-scale mesh, containing 378 elements.
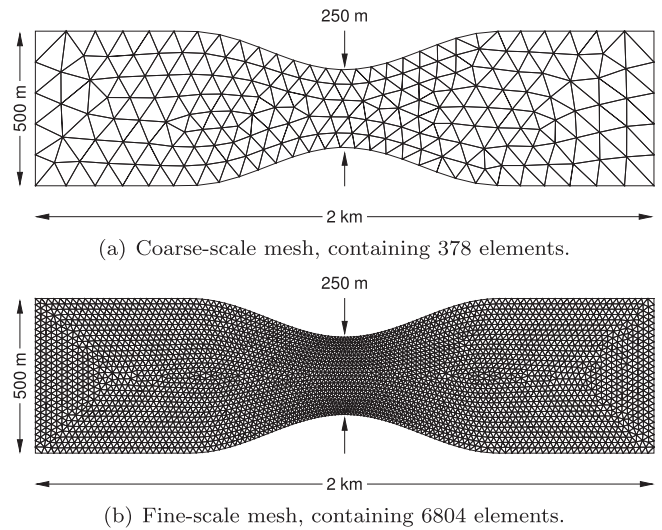

(b) Fine-scale mesh, containing 6804 elements.

Fig. 5. Unstructured computational meshes used in the converging channel test case. The ratio $h_{coarse}/h_{fine} \approx 4.88$, where h_{coarse} and h_{fine} are defined here as the longest edge lengths in the coarse and fine grids, respectively.

the purpose of calculating $\mathbf{q}_b$, the seawater density is taken as $\rho = 1024.763$ kg/m³, which is the value given by the UNESCO 1980 International Equation of State (IES-80; see [38] for details) with temperature $T = 20$°C and salinity $S = 35$ psu. For the hydrodynamics, nonlinear bottom friction given by $\tau_{bf} = c_f \|\mathbf{u}\|_2/H$ is considered, where c_f is the (dimensionless) friction coefficient or bed roughness, taken here to be 0.0025.

For purposes of comparison, this test case is run using two different grids. The first is a coarse mesh, shown in Fig. 5(a), and the second is a finer-scale mesh, shown in Fig. 5(b). For each of these grids, numerical realizations of $\mathbf{w}_h$ using piecewise constant, linear, and quadratic basis functions are considered. For the case of piecewise constant basis functions, time step sizes of 1.5 s (coarse grid) and 0.25 s (fine grid) are used with the Forward Euler scheme SSP (1,1); for piecewise linear basis functions, 0.75 s and 0.1 s, respectively, with SSP (2,2); for piecewise quadratics, 0.5 s and 0.1 s, respectively, with SSP (3, 3). Recall from Section 3.2 that a higher-order slope limiter described in [36] is applied when $p = 2$, which allows us to take slightly larger time step sizes than usual, though still well below the theoretical threshold given by the CFL condition. For example, using the estimate for the CFL restriction given by

$$\Delta t \leqslant \min_{\Omega_e} \left(\frac{h_e}{\left(\mathbf{u} \cdot \mathbf{n} + \sqrt{gH} \right)_e} \frac{1}{2p + 1} \right), \tag{19}$$

where h_e is defined here to be the longest (elemental) edge length, and $1/(2p + 1)$ is an estimate of the CFL number [16], we obtain $\Delta t_{CFL} \approx 0.85$ s for the coarse grid and $\Delta t_{CFL} \approx 0.15$ s for the fine grid. In practice, however, time step sizes of approximately $\Delta t_{CFL}/2$ must be taken before the model becomes stable when not utilizing a slope limiter; the ability to take time step sizes larger than $\Delta t_{CFL}/2$ is thus a welcomed feature of this slope limiter.

Plots of the bathymetry for $p = 0$, 1, and 2 on the coarse mesh at $t = 90$ days are shown in Fig. 6, while Fig. 7 shows the corresponding velocity magnitude. In Fig. 6, it can be seen that the bottom undergoes erosion in the converging part of the channel because the flow is accelerating there (shown in the corresponding figures for $\|\mathbf{u}\|_2$). Conversely, sediment accretion can be seen in the diverging part of the channel since the flow speed is decreasing there. The erosion and accretion patterns are not uniform across the width of
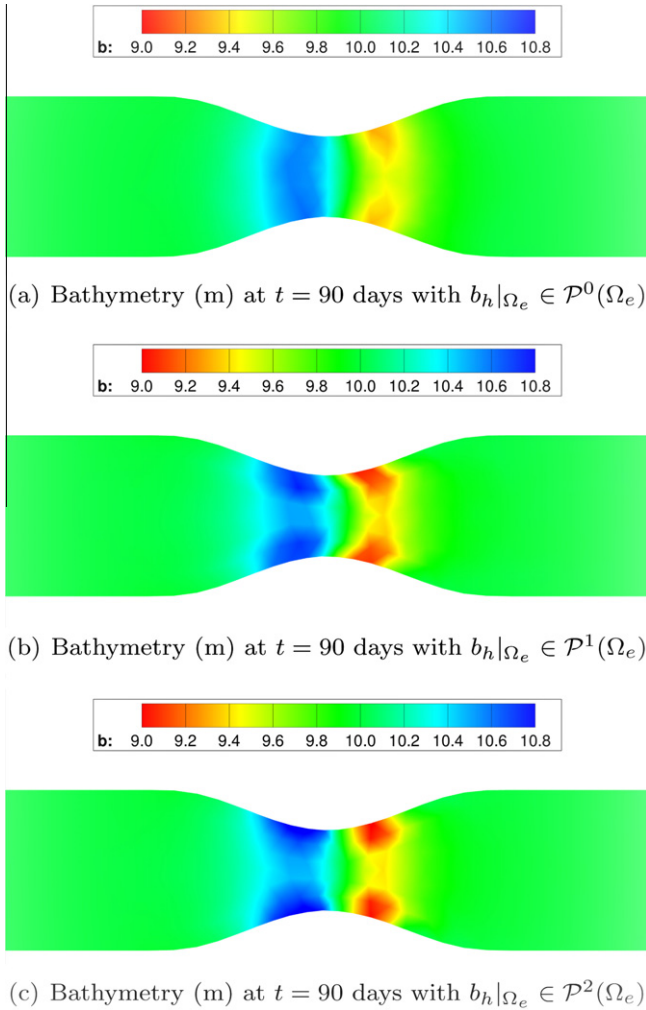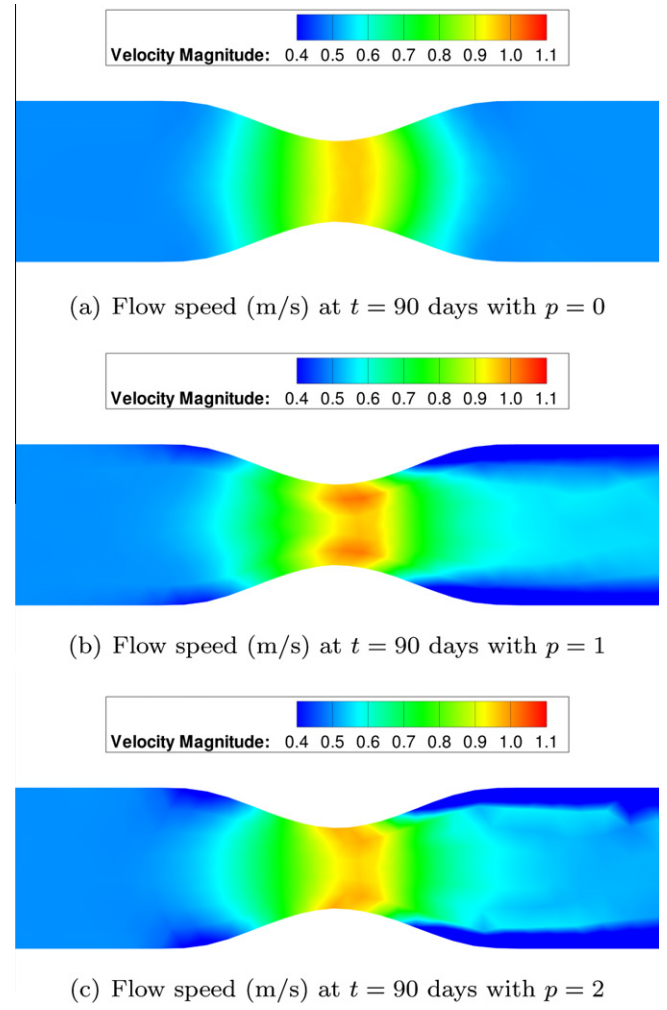
(a) Bathymetry (m) at $t = 90$ days with $b_h|_{\Omega_e} \in \mathcal{P}^0(\Omega_e)$

(b) Bathymetry (m) at $t = 90$ days with $b_h|_{\Omega_e} \in \mathcal{P}^1(\Omega_e)$

(c) Bathymetry (m) at $t = 90$ days with $b_h|_{\Omega_e} \in \mathcal{P}^2(\Omega_e)$

Fig. 6. Bathymetry (m) after 90 days on the coarse mesh.

(a) Flow speed (m/s) at $t = 90$ days with $p = 0$

(b) Flow speed (m/s) at $t = 90$ days with $p = 1$

(c) Flow speed (m/s) at $t = 90$ days with $p = 2$

Fig. 7. Flow speed (m/s) after 90 days on the coarse mesh.

the channel, however, as it can be observed in Fig. 7 that the velocity is nonuniform across the channel width; it is slightly higher near the center. Since the sediment transport rate $\mathbf{q}_b$ is a function of $\|\mathbf{u}\|_2^3$, the magnitude of the erosion and accretion is seen to vary considerably across the channel width.

The numerical solution exhibits qualitatively similar behavior on the fine-scale mesh, except with generally better resolution. Consider the bathymetric profiles shown in Figs. 6 and 8. For the piecewise constant case, notice that the fine-scale solution reflects higher sediment mass transport rates. For the cases of $p = 1$ and $p = 2$, differences in resolution are more pronounced: the solution on the fine mesh appears to better account for the land boundaries, and the resolution in the transition regions (on the upstream edge of the scouring region, between the erosion and deposition zones, and just downstream of the deposition region) is much sharper. The piecewise quadratic solution on the fine mesh (Fig. 8(c)) more sharply captures the transport behavior in the center of the channel; the cross-stream profile is not as well-resolved on the coarse mesh, especially in the accretion zone.

Now consider the velocity profiles shown in Figs. 7 and 9. For the case of $p = 0$, the fine-scale solution shows a slightly larger speed gradient, especially near the boundaries, explaining the differences in b_h between Fig. 6(a) and Fig. 8(a) as a result of the differing transport rates. For the cases of $p = 1$ and $p = 2$, one immediately spots the differences in the flow behavior near the land boundaries in the channel throat when comparing them with

the piecewise constant results. The increase in velocity from the channel center to the boundary region is more well-defined; this feature appears to be smeared in Fig. 7(b) and (c). The highest speeds occur nearer to the boundaries in the throat, and the velocity gradient downstream of the throat is much higher compared to the coarse-grid solution.

When $p \geqslant 1$, a long, thin boundary layer is seen downstream of the channel throat. Its appearance is consistent with the results shown in [13], and may be partly due to the effect of the no normal flow BC there (but free tangential slip is allowed). However, we note that by comparing Fig. 7(b) and Fig. 9(b), its thickness appears to depend on the grid size: as $h \to 0$, this layer becomes thinner, and appears to be confined only to those elements next to the land boundary.

Comparing the DG solutions for b and $\|\mathbf{u}\|_2$ across the different values of p, we immediately notice that the $p = 0$ approximation of b only superficially captures the scouring and accretion behavior; the computed sediment transport rate in the converging region appears too high, while it is too low along the land boundaries. Thus, some numerical diffusion is evident here; the $p = 0$ approximation of b appears to be overly diffusive. Increasing p dramatically improves the resolution of b_h, especially near the boundaries, in particular for $p = 2$, where the solution appears to sharply resolve the subgrid-scale features in the transition region. Fig. 6(b) and Fig. 8(c) show that the higher-order slope limiter suppresses oscillations near the land boundaries in the throat of the channel
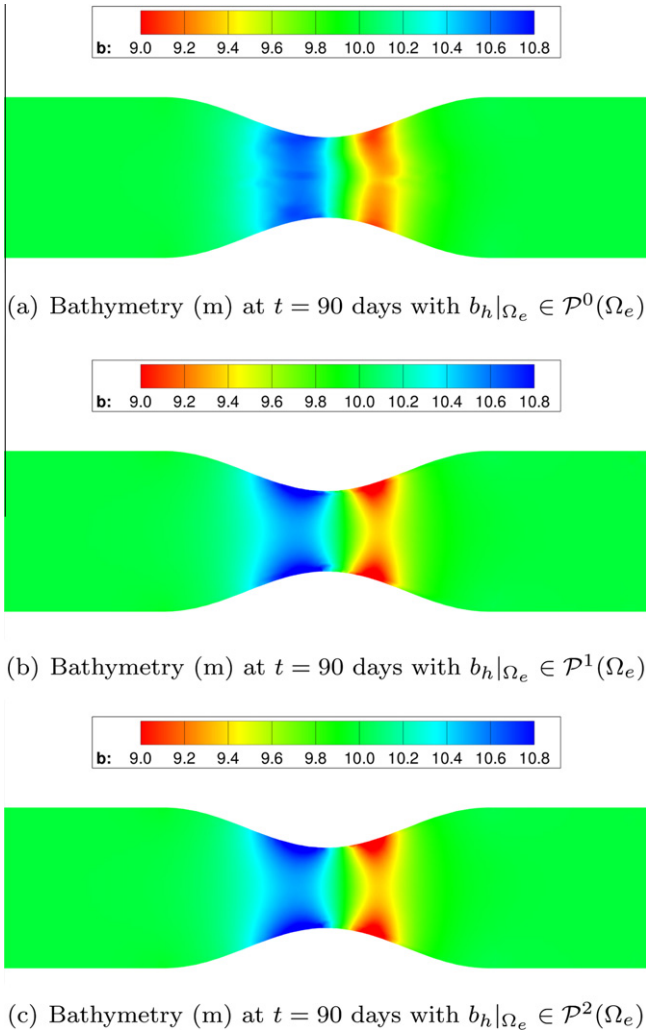
(a) Bathymetry (m) at $t = 90$ days with $b_h|_{\Omega_e} \in \mathcal{P}^0(\Omega_e)$
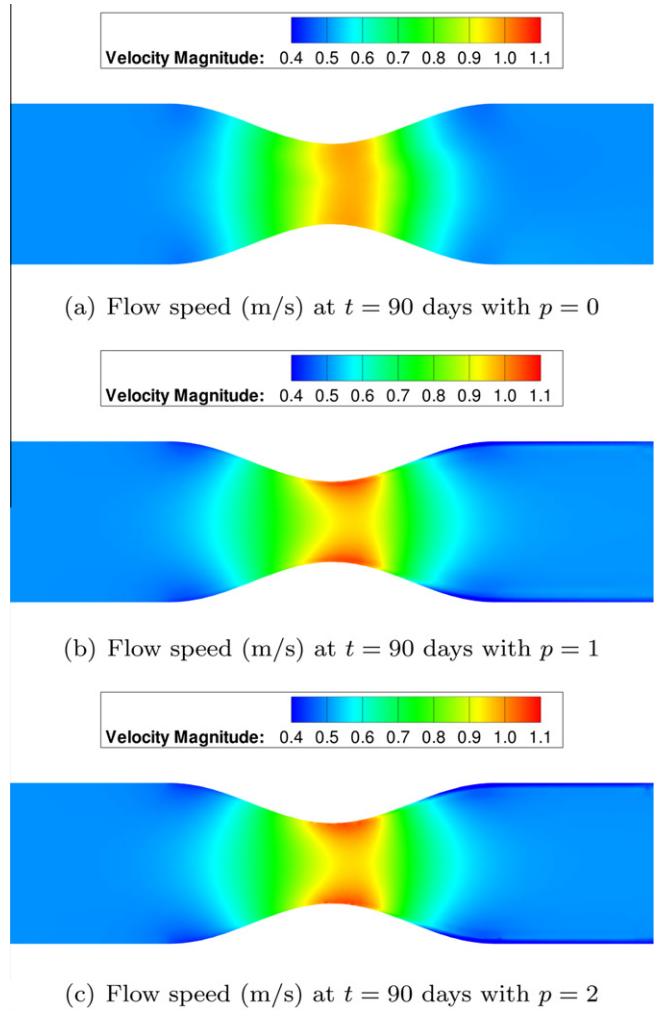
(b) Bathymetry (m) at $t = 90$ days with $b_h|_{\Omega_e} \in \mathcal{P}^1(\Omega_e)$

(c) Bathymetry (m) at $t = 90$ days with $b_h|_{\Omega_e} \in \mathcal{P}^2(\Omega_e)$

Fig. 8. Bathymetry (m) after $t = 90$ days on the fine mesh.

(a) Flow speed (m/s) at $t = 90$ days with $p = 0$

(b) Flow speed (m/s) at $t = 90$ days with $p = 1$

(c) Flow speed (m/s) at $t = 90$ days with $p = 2$

Fig. 9. Flow speed (m/s) after $t = 90$ days on the fine mesh.

when $p = 2$. Turning our attention to $\|\mathbf{u}\|_2$, we find a similar problem of resolution when $p = 0$: the cross-stream velocity profile appears to be nearly uniform in the throat of the channel, and the model fails to capture the behavior of the solution near the land boundaries in the channel throat; the predicted speed still appears to be too low.

Based on the issues pointed out thus far, it should be noted that the coarse-grid solutions do not seem to be satisfactory for any value of $p \in \{0,1,2\}$ when compared with some results shown in the literature [13,25]. Results obtained using the fine-scale grid are still not well-resolved when $p = 0$, but are generally very well-resolved when $p \geqslant 1$. These observations, especially the final one, underscore the need for taking p of sufficient order in the DG approximations.

It is important to observe the interaction between the bathymetric and velocity profiles as both evolve in time: as the bed is eroding in the converging part of the channel, the total depth H increases, which in turn acts to decrease $\|\mathbf{u}\|_2$. Conversely, as a mound begins to form on the bed in the diverging part of the channel, H decreases, causing an increase in $\|\mathbf{u}\|_2$ in this region. This ongoing (coupled) process results in the entire velocity profile slowly shifting slightly downstream with time. These results are shown in Figs. 10 and 11.

Lastly, it should be noted that the results shown in Figs. 6–9 all compare well qualitatively with an analytical solution derived by Exner in [4] for a problem with similar geometry, with results

shown in Tassi et al. [13] for this problem posed in a non-dimensional setting, and with the computed results presented in Kubatko et al. [25] using a combined CG-DG model (for $p = 1$).

4.3. Scouring around a Bridge Pier

In this section, another well-known and well-studied problem in coastal engineering is examined: scouring, or bed erosion, around a vertical, cylindrical bridge pier, such as those commonly seen on roadway and railway bridges across rivers and estuaries. Applications of these problems to coastal engineering activities motivate our model testing here, as scouring has been cited as one of the most common causes of bridge failures in these regions [8,39]. We also wish to verify that our model accurately depicts the major flow features associated with the scouring process, at least in a qualitative sense. This problem would be more accurately simulated by a three-dimensional Navier–Stokes model, but an interesting question is to determine which features can be captured by a hydrostatic, depth-averaged model.

In this problem, an initially flat bed is subjected to a uniform, unidirectional flow originating from the western (upstream) boundary. This free stream or upstream velocity is denoted as $\mathbf{u}_\infty = (u_\infty, 0)^T$. The domain under study in this test case is a square of side length 30 m with a circular island of diameter $D = 2$ m positioned at the origin. However, since the true solution $\mathbf{w}$ is symmetric about the x-axis, our domain is chosen as
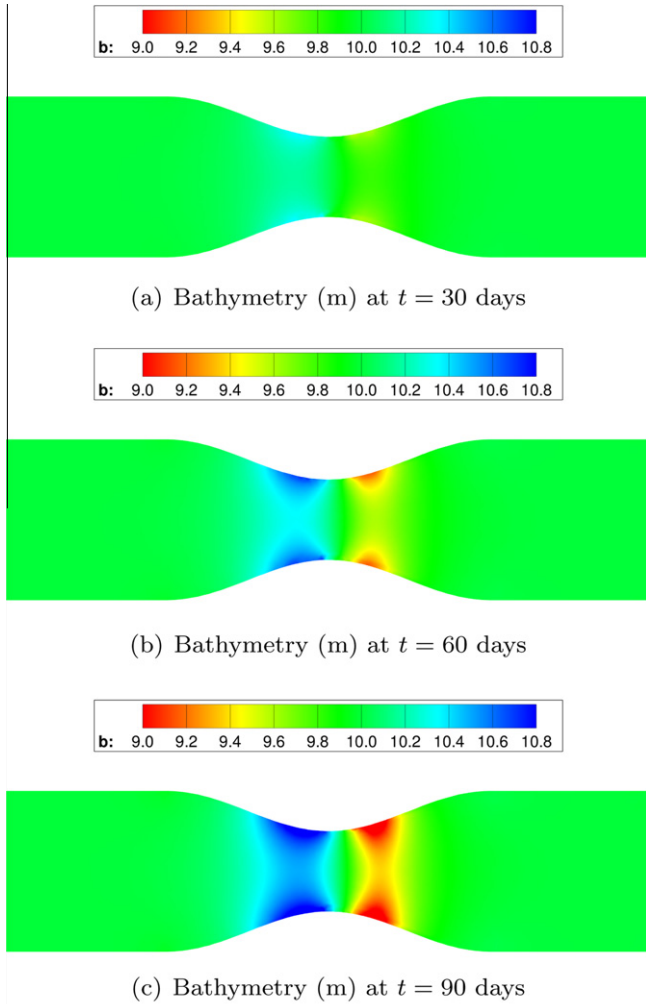
(a) Bathymetry (m) at $t = 30$ days

(b) Bathymetry (m) at $t = 60$ days

(c) Bathymetry (m) at $t = 90$ days

Fig. 10. Bathymetry (m) at 30-day intervals on the fine mesh with $p = 2$.

(a) Flow speed (m/s) at $t = 30$ days

(b) Flow speed (m/s) at $t = 60$ days

(c) Flow speed (m/s) at $t = 90$ days

Fig. 11. Flow speed (m/s) at 30-day intervals on the fine mesh with $p = 2$.

$$\Omega = \{(x,y) \in \mathbb{R}^2 : x \in (-15, 15),\ y \in (0, 15),\ x^2 + y^2 > 1\}$$

in order to save computational time. Two computational meshes shall be used for this test case for comparison. These are shown in Fig. 12. The bed is initially flat with a depth of 1 m. Boundary conditions are similar to those for the previous test case, and are as follows: at $x = -15$, the velocity is fixed at $u_\infty = 0.2$ m/s. At the bridge pile boundary, a no normal flow boundary condition is imposed. No normal flow is also imposed at the top ($y = 15$) and along the axis of symmetry ($y = 0$). At $x = 15$, the free surface elevation is specified as $\zeta = 0$. Values for ε_0, ρ_s, d_{50}, ρ, and c_f are the same as for the test case in Section 4.2. However, in order to save computational time, the sediment transport rates are artificially inflated by a factor of 1000 so that the bed evolution may be examined after 1 day, well after the flow becomes fully-developed.

Following the pattern begun with the previous test cases, we seek $\mathbf{w}_h|_{\Omega_e} \in \mathcal{P}^p(\Omega_e)$ for $p = 0$, 1, and 2 for both meshes. When $p = 0$, the time step sizes are set to 0.025 s (coarse mesh) and 0.01 s (fine mesh) and SSP (1,1) is employed; $p = 1$, 0.01 s and 0.005 s, respectively, with SSP (2,2); $p = 2$, 0.0075 s and 0.0025 s, respectively, with SSP (3,3). Recall from Section 3.2 that the slope limiter described in [35] is applied to all components of $\mathbf{w}_h$ in order to control and/or suppress oscillations when $p = 1$. For the piecewise quadratic case, the WENO-type limiter described in [36] is used, again for the purpose of enforcing some form of TVB stability.

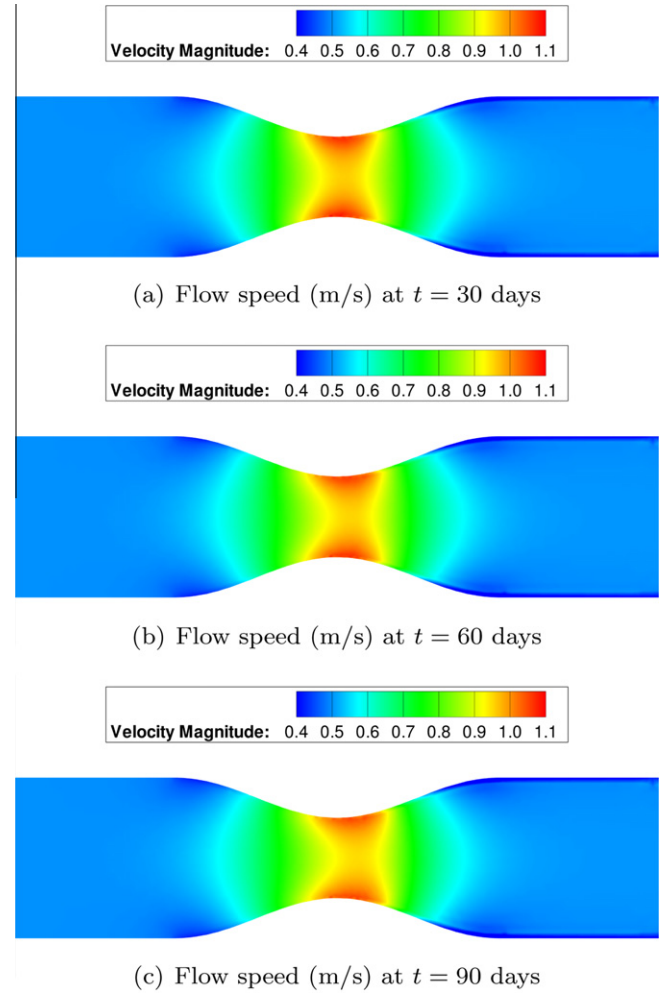For this problem, experimental results show that the basic scouring process and flow profile evolution may be summarized as follows. The initial approach flow splits in the horizontal direction when reaching the pier into an upper and lower flow, leaving a stagnation point at the head of the pier (the point $(-1, 0)$ in our domain). A corresponding stagnation pressure results; fluid approaching the stagnation point decelerates, causing some pileup (and thus an increase in ζ) [39] and a bow wave, and then accelerates along the sides of the pier [40]. The fully-developed flow speed along the pier perimeter reaches its maximum at an angle $\theta \approx 75°$ from the pier head, but then separates in the region $90° \leqslant \theta \leqslant 120°$ as a result of the acceleration along the sides [41], and a long wake results. Meanwhile, scouring of the bed is initiated near $\theta \approx 75°$, closely corresponding to the point where the (attached) accelerating flow reaches its maximum speed [41]. Sediment accretion occurs just downstream of the pier, and the mound slowly drifts downstream with time because of the growing scour hole [41].

However, it should be noted that in addition to this, the approach flow also splits in the vertical direction at the upstream stagnation point; the up-flow contributes to the formation of the bow wave, while the down-flow forms a vertical eddy or vortex [40]. Because of accelerating flow around the pile, a horseshoe vortex system is subsequently formed, and this has been deemed to be the main scouring agent upstream of the pier [40,41]. Thus, in time, the scour hole advances upstream, eventually becoming U-shaped [40]. We note that this latter process is inherently a three-dimensional effect, and consequently we cannot hope to properly simulate it with our two-dimensional model. We proceed with this caveat in mind.
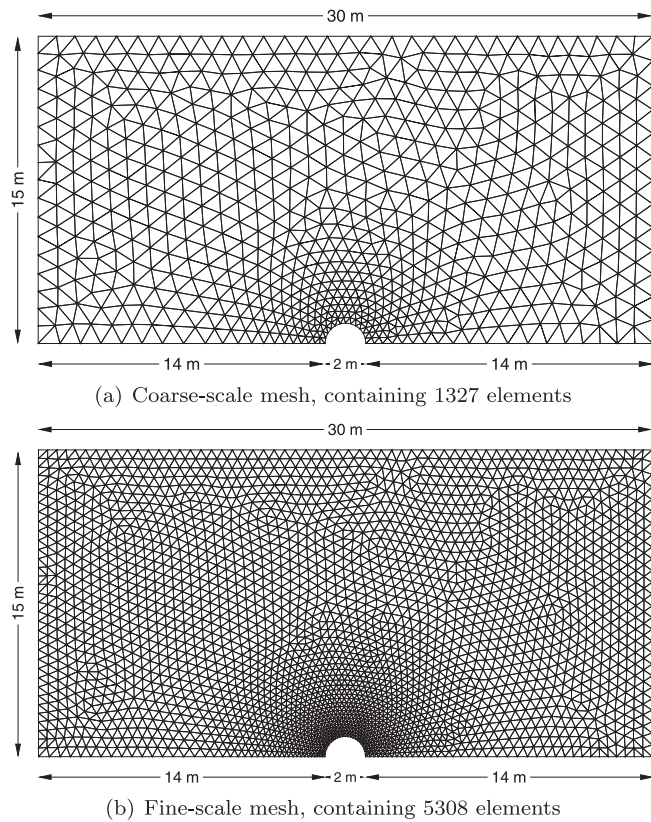
(a) Coarse-scale mesh, containing 1327 elements

(b) Fine-scale mesh, containing 5308 elements

Fig. 12. Unstructured computational meshes used for the bridge pier scouring test case. The fine-scale mesh (b) is a uniform 1:4 refinement of the coarse-scale mesh (a).

The resulting bed profiles are shown in Fig. 13 for the coarse-scale mesh and in Fig. 15 for the fine-scale mesh. The corresponding velocity profiles are displayed in Fig. 14 for the coarse-scale mesh and in Fig. 16 for the fine-scale mesh. In all results, the locations of the stagnation points, scouring initiation points, points of maximum flow speed along the perimeter, and flow separation points appear to be in good agreement with the results presented in [39,41].

In Figs. 13 and 15, it can be seen that scouring emanates from a point on the pier perimeter near $\theta = 75°$, which agrees with experimental data in [41], and then is deposited just downstream of the pile, as should be expected. However, the extent of the scouring varies considerably between the coarse- and fine-scale meshes, especially when $p \geqslant 1$; h-refinement near the bridge pier appears to play a significant role here in the accurate calculation of the sediment transport rate. Also, when $p \geqslant 1$, the resolution of the scour hole seems to be slightly improved, and its extent appears to be reduced. The same may be observed with the corresponding velocity profiles: the wake appears slightly sharper and more compact (although the flow seems to separate slightly too far downstream compared to the coarse-scale solution, which shows separation around $\theta = 120°$), as does the flow near the upstream stagnation point.

By closely observing the differences in the scouring and accretion profiles when $p \geqslant 1$, the following may be noted. When $p = 1$, differences between the coarse- and fine-scale solutions are quite apparent; the coarse-grid scour hole appears smeared, and simply emanates outward at $\theta \approx 75°$, while the fine-grid hole exhibits a downstream tail. Its visual appearance is similar to that of the $p = 2$ coarse-grid solution. While the corresponding fine-grid solution for $p = 2$ shown in Fig. 16(c) displays some additional structure, it is not substantially qualitatively different. Conse-
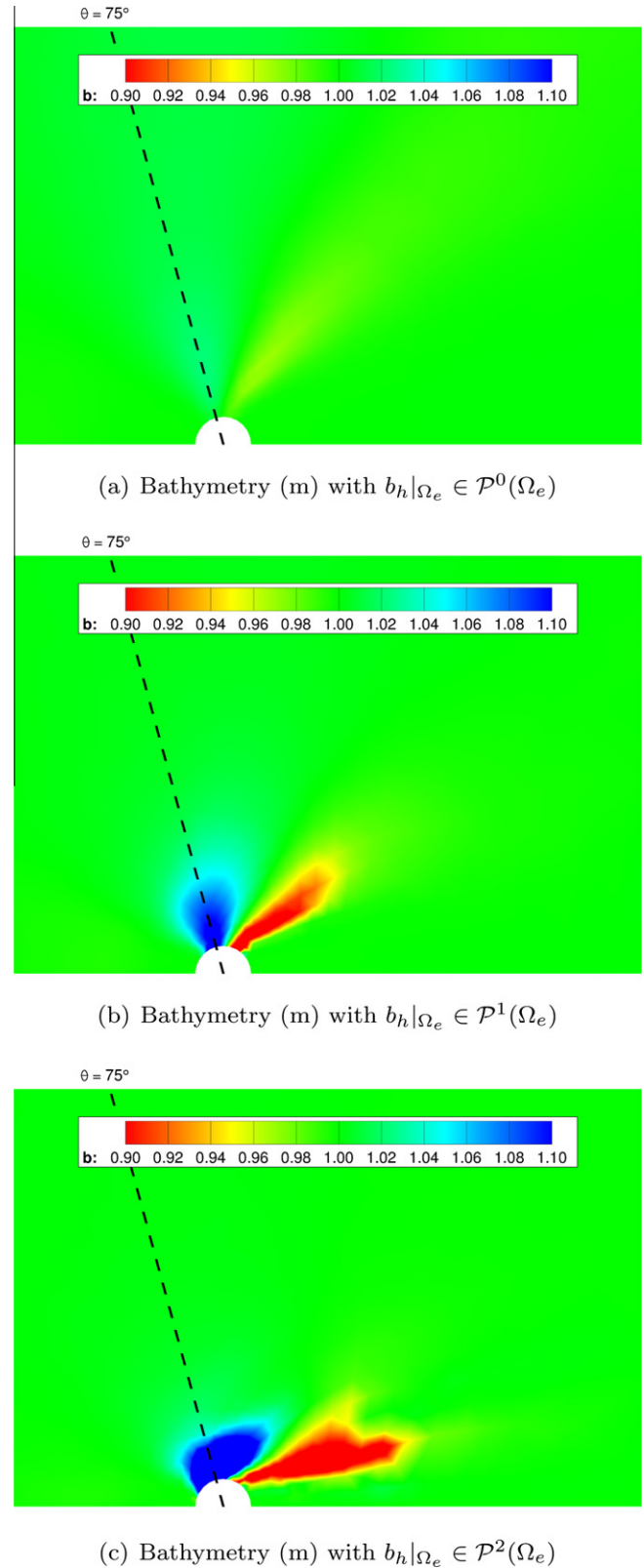

(a) Bathymetry (m) with $b_h|_{\Omega_e} \in \mathcal{P}^0(\Omega_e)$

(b) Bathymetry (m) with $b_h|_{\Omega_e} \in \mathcal{P}^1(\Omega_e)$

(c) Bathymetry (m) with $b_h|_{\Omega_e} \in \mathcal{P}^2(\Omega_e)$

Fig. 13. Bed profiles after 1 day on the coarse mesh.

quently, the piecewise quadratic approximations to b may possibly be showing some signs of convergence (although additional trials would be needed to verify this).

Many differences in the bed evolution can be remarked upon among the cases for $p = 0$, 1, and 2. For the piecewise constant case,
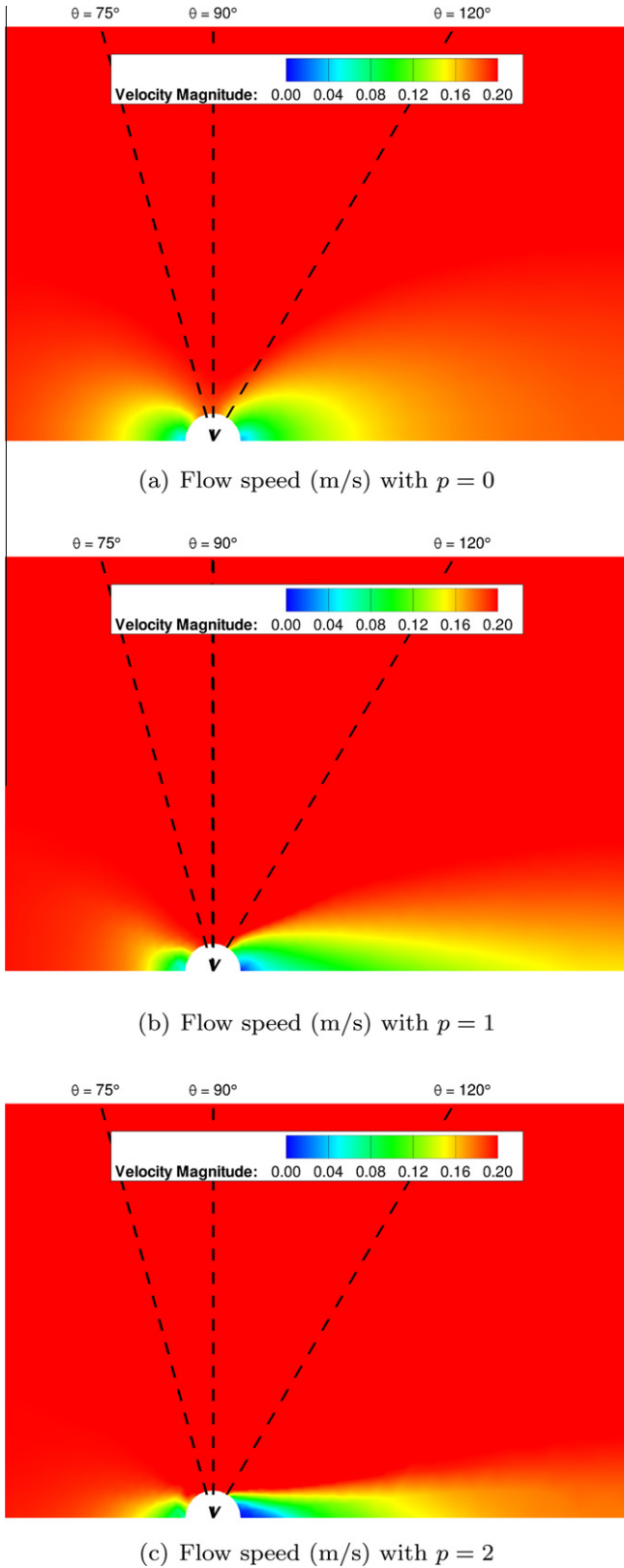
(a) Flow speed (m/s) with $p = 0$

(b) Flow speed (m/s) with $p = 1$

(c) Flow speed (m/s) with $p = 2$

Fig. 14. Velocity profiles after 1 day on the coarse mesh.

(a) Bathymetry (m) with $b_h|_{\Omega_e} \in \mathcal{P}^0(\Omega_e)$

(b) Bathymetry (m) with $b_h|_{\Omega_e} \in \mathcal{P}^1(\Omega_e)$

(c) Bathymetry (m) with $b_h|_{\Omega_e} \in \mathcal{P}^2(\Omega_e)$

Fig. 15. Bed profiles after 1 day on the fine mesh.

notice that the eroding and accretion regions extend nearly two-thirds of the way to the domain boundary. This is clearly unrealistic, since both experimental and analytical investigations suggest that the boundary of the scour hole lies much closer to the pile [40]. Thus, the RKDG scheme with $p = 0$ seems to be much too dif-

fusive, and this demonstrates the need for increasing p to sufficient order. Also, the maximum scour and sediment accumulations are far less than the maxima attained for the other two cases, possibly indicating that the calculated sediment transport rates may be too low. This agrees with our observations in Section 4.2. When p is increased to one, a more realistic result emerges, as the area of
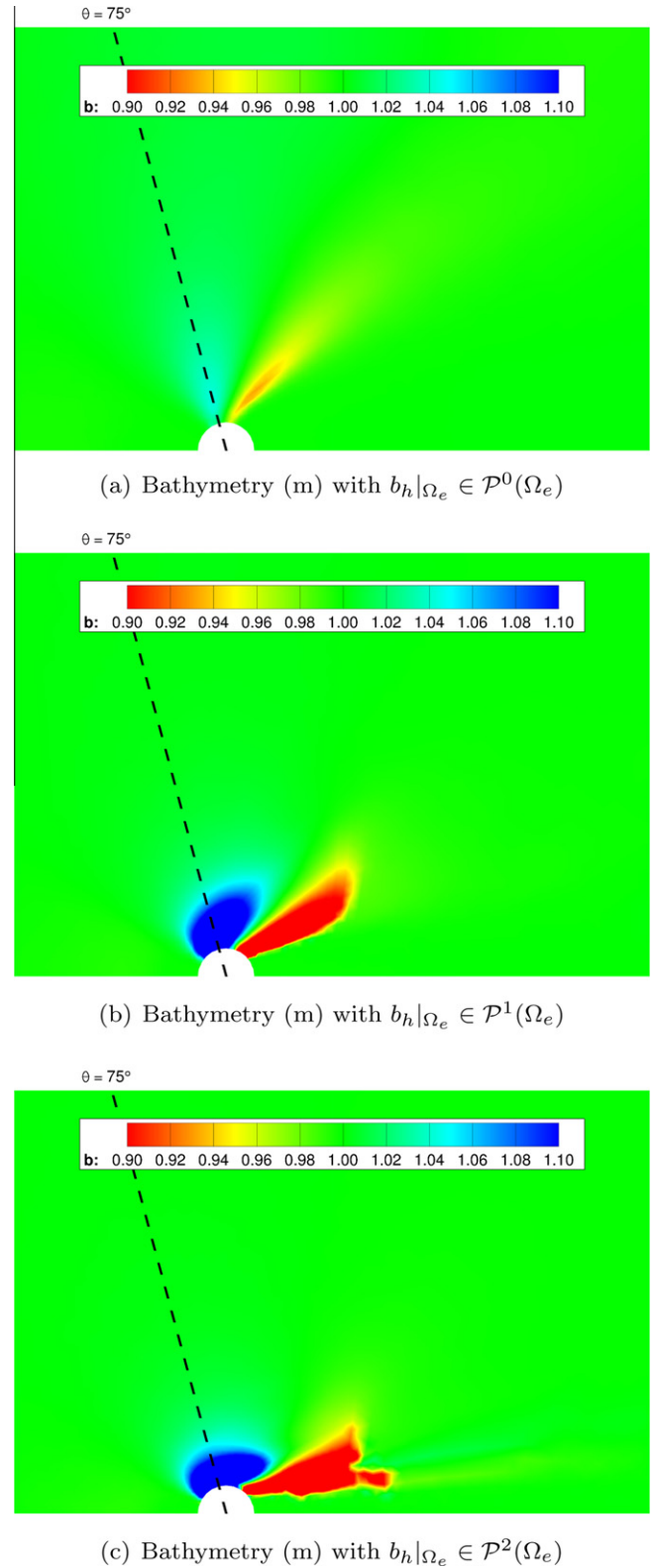
(a) Flow speed (m/s) with $p = 0$

(b) Flow speed (m/s) with $p = 1$

(c) Flow speed (m/s) with $p = 2$
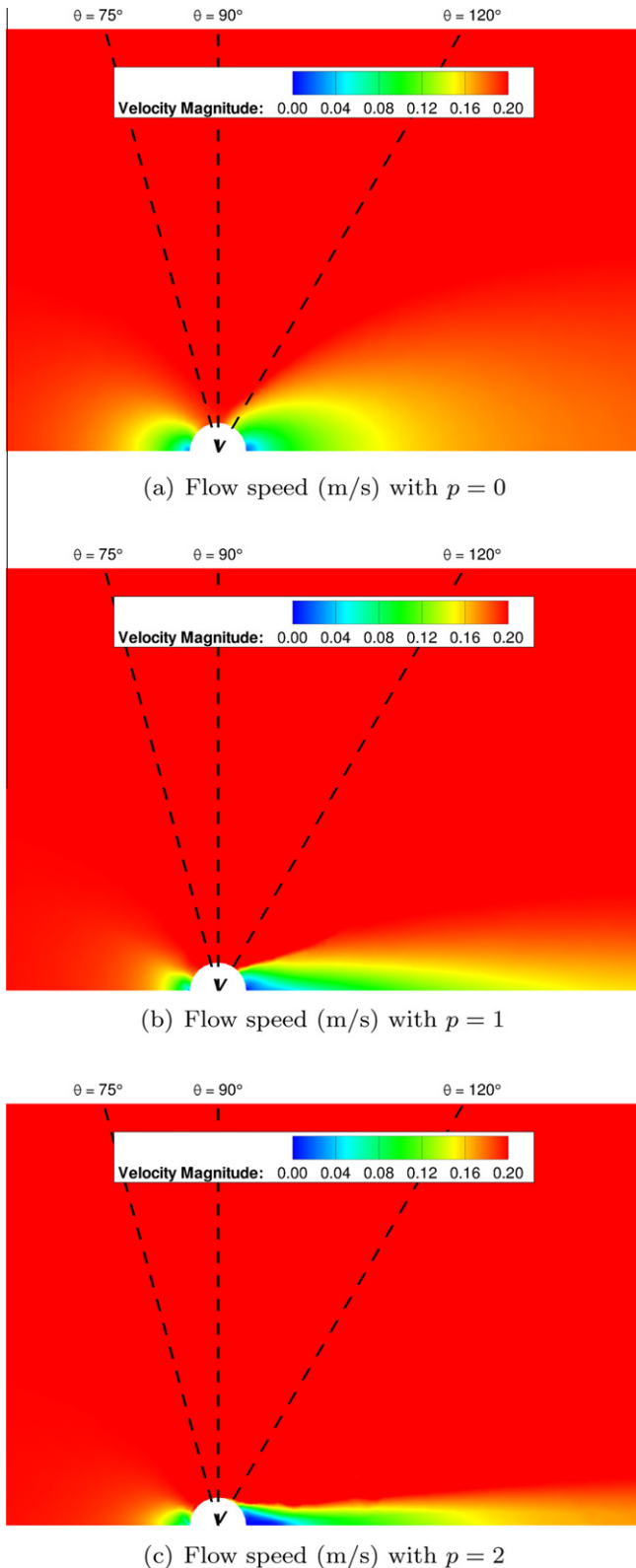
Fig. 16. Velocity profiles after 1 day on the fine mesh.

erosion and deposition is constrained to a distance not exceeding approximately 2D. The higher scouring and accretion rates may be attributed to the larger velocity gradients seen in Figs. 14(b) and Fig. 16(b), especially in the wake, whose width is now much smaller; it is not smeared. The piecewise quadratic solutions appear even less diffusive, even with the use of the higher-order

slope limiter: an even larger amount of sediment pick-up occurs in a still smaller scour hole located closer to the pier compared with the $p = 1$ case, and the ends of the U-shape attained by the scour hole are more evident. The wake and upstream stagnation regions are more compact as well. Additionally, observe that the accretion region emanates outward at a larger angle θ as p is increased. It should be noted, however, that the general lack of diffusion seen in these results for $p \geqslant 1$ is primarily a numerical phenomenon, and it is a consequence of our decision to ignore the diffusive terms in Eqs. (1a), (1b) and (2); some physical diffusion will be seen in reality.

Lastly, we note that examination of the elevation profile for all model runs revealed strong numerical evidence of a bow wave, as values of ζ were elevated near the upstream stagnation point where seawater pileup is expected. However, for the sake of brevity, we do not show these results here.

4.4. An idealized inlet

We now turn our attention toward a coastal modeling application. In this test case, an idealization of a typical coastline, channel, and bay or estuary is considered. For this case, we wish to ensure that the model properly captures the twin eddy formation in the back bay during an incoming (flood) tide, the corresponding formation in the ocean during an outgoing (ebb) tide, the formation of an ebb shoal in the ocean off the ends of the jetties, and the formation of a corresponding flood shoal in the back bay. Ebb and flood shoal formation is very common in both coastal inlets and river deltas, and they form as a result of sediment accretion caused by decelerating flow exiting the channel during the ebb and flood tides, respectively. Though the time scales are generally on the order of months to many years (assuming fair weather), this process, left unchecked, can severely alter the flow patterns of an inlet and disrupt shipping operations, and the ensuing dredging operation may be very expensive. Thus, analysis of these systems serves an important purpose. An example of an ebb and flood shoal is shown in Fig. 17.

The domain under consideration here is shown in Fig. 18. It is a simplified, or idealized, inlet containing a channel 300 m wide and 525 m long which connects a rectangular section (stretching 3 km north to south and 2.475 km out to sea) of open ocean to the west with a rectangular back bay (spanning 3 km north to south and 1.5 km inland) to the east. At the western end of the channel are twin jetties 50 m wide and 225 m long. The initial bathymetry in the back bay and channel is flat and measures 5 m, while the bottom slopes linearly in the open ocean to the west, measuring 19 m at the western open ocean boundary. The water in the sea, channel, and back bay is initially tranquil.

The boundary conditions for this problem are as follows: a no normal flow condition is imposed at the northern, southern, and eastern edges of the open ocean, as well as at the jetties, channel walls, and all edges of the back bay. On the western open ocean boundary, we specify a spatially uniform periodic flow rate, with an amplitude of $\mathbf{q}^{(ex)} = (0.75, 0)^T$ m²/s, and a frequency corresponding to that of the M_2 tide (period 12^{h}25^{m}14^s). This amplitude was chosen so that the maximum flow speed in the channel is approximately 1 m/s.

This test case is solved over a period of 10 days using piecewise constant, linear, and quadratic basis functions for the purpose of comparison. For the piecewise constant approximation, a time step size of 1.25 s with SSP (1,1) is used; for the piecewise linear approximation, 0.5 s with SSP (2,2); for the piecewise quadratic approximation, 0.25 s with SSP (3,3). Recall once more from Section 3.2 that for the sediment transport equation, the slope limiter of Cockburn and Shu [35] is applied when $p = 1$, and the higher-order slope limiting procedure of Xu et al. [36] is applied when $p = 2$.
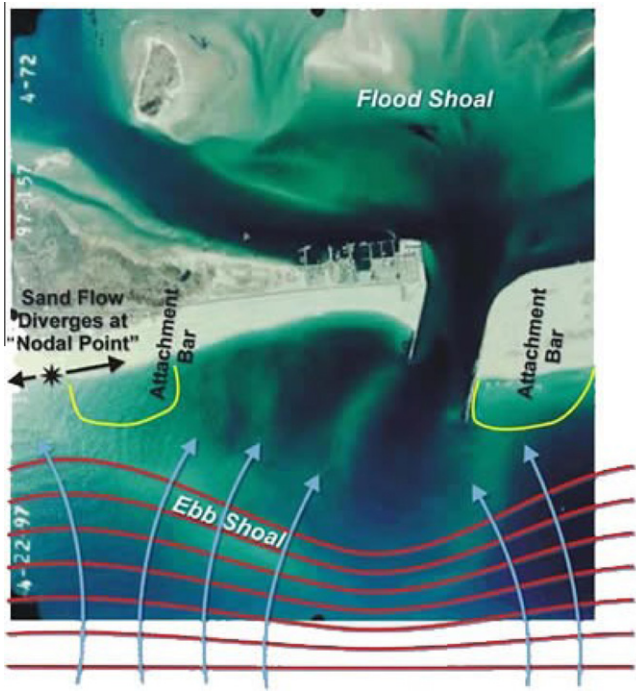
Fig. 17. A photographic description of ebb and flood shoal formation in Shinnecock Inlet, NY, USA. Photograph courtesy NOAA Coastal Services Center.
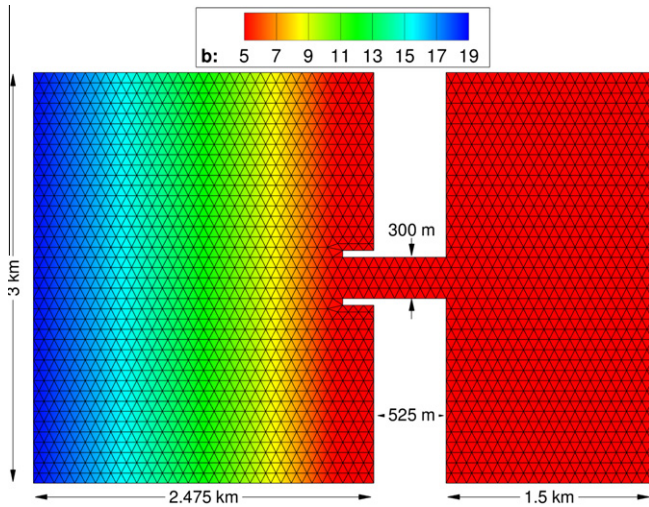

Fig. 18. Computational domain of the idealized inlet system containing 4374 elements. The initial bathymetry (m) is shown as well. The jetties are 225 m long by 50 m wide.

The bed remains non-porous, with the same values for d_{50} and ρ as in Section 4.2. However, the grain density is now increased to 2650 kg/m^3. The nonlinear bottom friction coefficient c_f is increased to 0.003 for this case. Additionally, the sediment transport rates were magnified 50 times in order to speed up the bed evolution process. This was done in the interest of saving computational time.

Fig. 19(a), (b), and (c) show plots of the piecewise constant, linear, and quadratic approximations of b after 10 days, respectively, in the vicinity of the channel. The other areas of the domain experience negligible amounts of sediment transport, and so are not shown here; the most interesting flow features are found in the channel region. The most prominent of these is the formation of
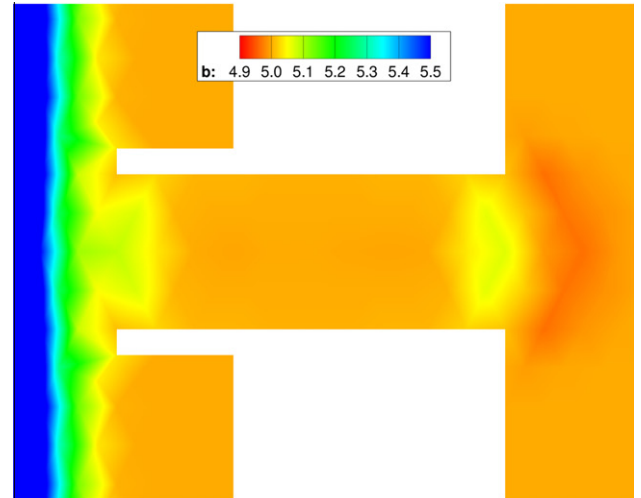
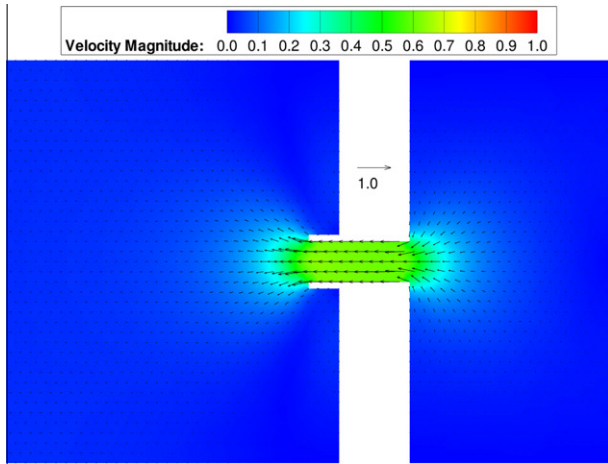(a) Bathymetry (m) with $b_h|_{\Omega_e} \in \mathcal{P}^0(\Omega_e)$
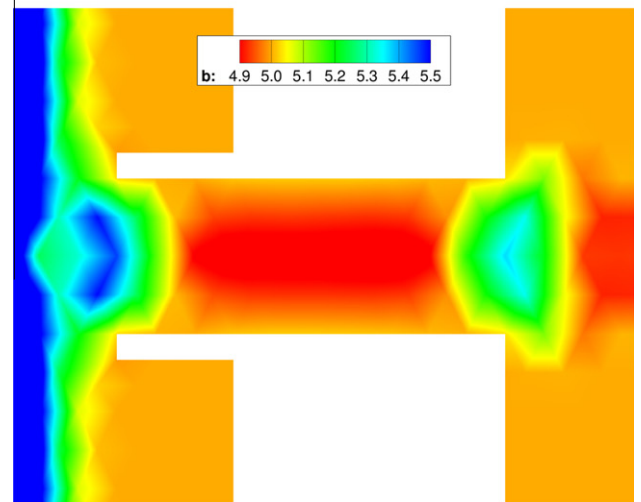
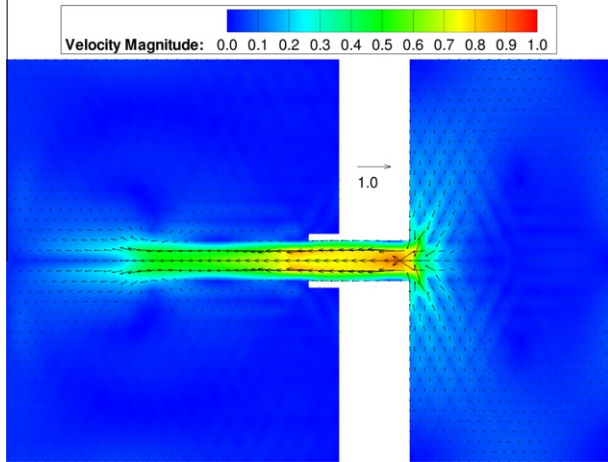(b) Bathymetry (m) with $b_h|_{\Omega_e} \in \mathcal{P}^1(\Omega_e)$
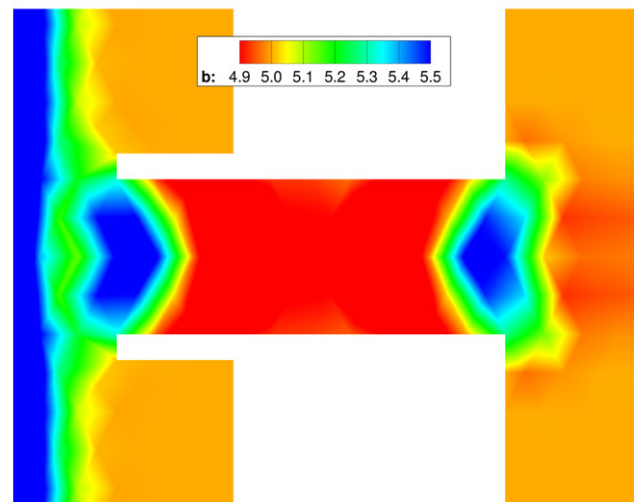
(c) Bathymetry (m) with $b_h|_{\Omega_e} \in \mathcal{P}^2(\Omega_e)$

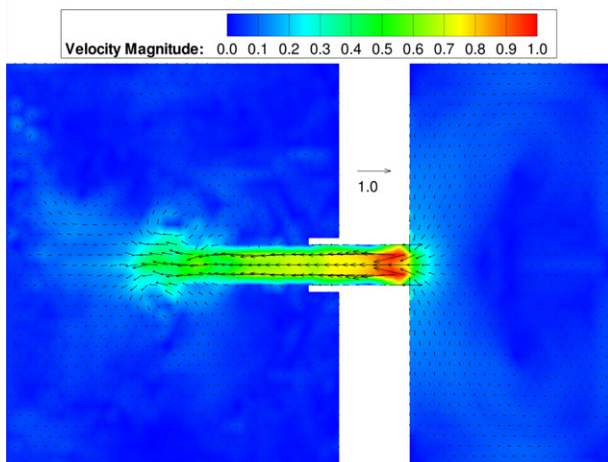Fig. 19. Bathymetry (m) in the channel region at t = 10 days.

dual scour holes in the center of the channel—one located at the entrance to the back bay, the other just off the ends of the twin jet-
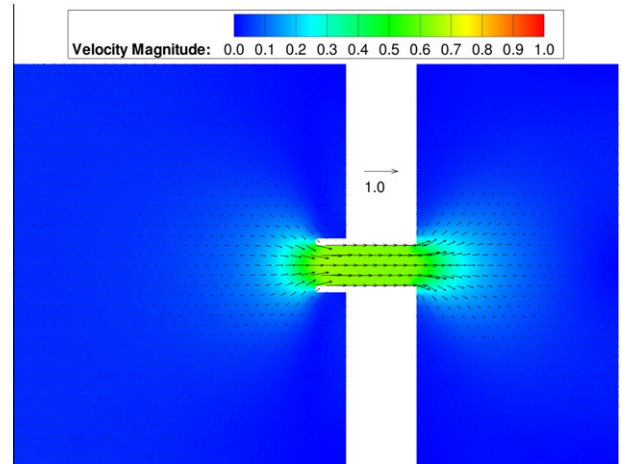
(a) Velocity profile (m/s) with $p = 0$
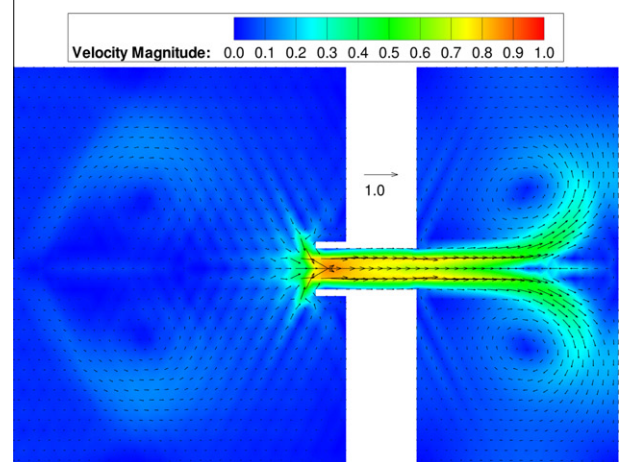
(b) Velocity profile (m/s) with $p = 1$
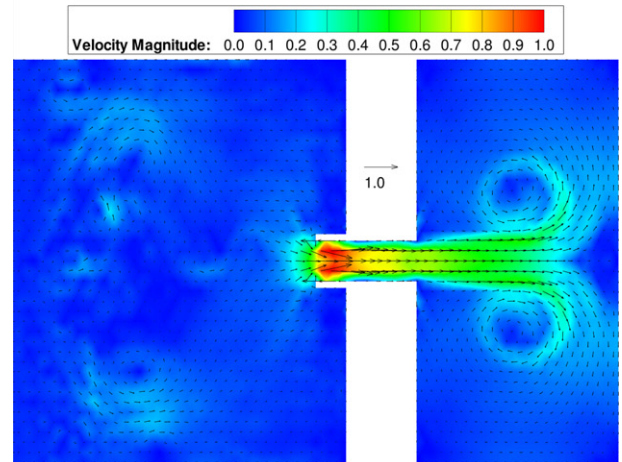
(c) Velocity profile (m/s) with $p = 2$

Fig. 20. Velocity profiles during approximate maximum ebb.

(a) Velocity profile (m/s) with $p = 0$

(b) Velocity profile (m/s) with $p = 1$

(c) Velocity profile (m/s) with $p = 2$

Fig. 21. Velocity profiles during approximate maximum flood.

ties. These scour holes are caused primarily by converging accelerating flow during the incoming tide (for the hole near the jetties) and during the outgoing tide (for the hole at the bay entrance). This dual scour hole formation is consistent with what is observed in real channel-inlet systems, such as Shinnecock Inlet, NY, where bathymetric soundings reveal dual scour holes in approximately the same locations as described above (though these are slightly off-center because the channel is not straight, as can be seen in

Fig. 17). The jagged shape of the scour holes is a direct result of the relative coarseness of the mesh in this region (see Fig. 18); this grid size was chosen as a compromise between resolution and computational time.

Notice also in Fig. 19(b) and (c) that sediment accretion occurs in the center of the channel. This phenomenon is due to the slightly negative velocity gradient existing there for most of the duration of the M_2 tidal cycle. See Figs. 20 and 21, and observe the channel center. These results suggest a mechanism by which channels could fill in over longer time periods and possibly block the flow, posing a hazard to shipping interests, however, this requires further investigation. Finally, we notice the formation of ebb and flood shoals beyond the scour holes, which are also caused in part by the negative velocity gradients in these regions during the ebb and flood tides, respectively.

Comparing the results across the different values of p, we remark that the piecewise constant approximation to b once again fails to capture the full extent of the induced bed evolution: the scour hole depths are approximately 9 cm and 7 cm at the jetties and back end, respectively, compared with 49 cm and 36 cm for the piecewise linear case and approximately 55 cm (both ends) for the piecewise quadratic case. It should be noted, however, that values for the scour hole depths for $p \geqslant 1$ are highly dependent on the use of the slope limiter; it should be made clear that without the use of a slope limiter, runaway scouring will eventually occur, and the resulting scour hole depths will become non-physically large, leading to numerical instability. In any case, the depths were substantially higher than those obtained when $p = 0$.

The maximum speed in the channel is approximately 0.2 m/s lower when $p = 0$ compared with $p > 0$, and since the transport rate depends on $\|\mathbf{u}\|_2^3$, the induced transport rate of sediment is lower. Low deposition rates for this case result in scant evidence of ebb and flood shoal formation, and of accretion in the channel center. These low observed rates of sediment transport compared to higher-order approximations are again consistent with what was seen in Sections 4.2 and 4.3.

Seeking a higher-order approximation of $\mathbf{w}$ yields a dramatic improvement in resolution, as numerical evidence for ebb and flood shoal formation is clearer, and sediment accretion in the center is more easily seen. The solution for the case of $p = 2$ appears to be even less diffusive; the scour holes are now very well-defined, as is the accretion in the channel center.

For this test case, as alluded to earlier, it is worthwhile to examine the velocity profiles at two different times—during the approximate time of maximum ebb, which is the time in which the seaward current associated with the outgoing tide is the strongest, and during the approximate time of maximum flood, when the incoming tidal current is the strongest. Fig. 20 shows the flow profile for $p = 0$, 1, and 2 at maximum ebb. Immediately it is seen that the numerical solution for the piecewise constant approximation to $\|\mathbf{u}\|_2$ is unrealistically simple; the model cannot resolve the dual eddies that form in the ocean as a result of interaction with the jetties. Even within the channel, the grid- and subgrid-scale flow features are not well-resolved. This changes drastically when $p \geqslant 1$, as Fig. 20(b) reveals two sets of dual eddies. One of these is a pair of jetty-scale eddies appearing in the ocean near the leading edge of the main seaward current coming from the channel. A pair of kilometer-scale eddies in the back bay is present as well, and these are residual eddies which contain remnants of the seawater transported into the bay during the previous incoming tide. They supply the seawater mass for the return flow. The $p = 2$ solution appears to give slightly better resolution of these large-scale eddies. Notice also that the solutions for $p \geqslant 1$ reveal much greater detail within the channel, especially near the scour holes, where small regions of increased velocity are seen. In addition, long, thin tails of slow-moving seawater are present near the channel walls—a feature

not seen in the $p = 0$ case, but consistent with results shown in [16]. Grid- and subgrid-scale velocity gradients are better resolved here, too, specifically in the piecewise quadratic case. All of these observations underscore the need to take $p \geqslant 1$ in order to obtain a reasonable flow profile.

The velocity profiles for the opposite tidal phase are shown in Fig. 21. Similar remarks from the previous paragraph about the solutions for the different values of p apply here as well: the numerical solution for $p = 0$ is still far too simplistic, while the piecewise linear approximation only partially resolves the (now clearly visible) dual eddies in the back bay, which appear to be nearly fully resolved only when $p = 2$ (shown in Fig. 21(c)). These observations and results are consistent with those in [16]. Note, however, that during the flood tide, a pair of unnatural residual kilometer-scale eddies remain in the ocean, which is likely a result of the interaction between the outgoing current (originating from the channel) and the flow-specified western boundary: they likely are deflected back into the domain and do not dissipate quickly enough since Eqs. (1b) and (2) neglect diffusion terms. This not only highlights the issues relating to numerical diffusion, or lack thereof, but also highlights the ongoing issue of proper specification of open ocean boundary conditions in the framework of the DG method, which were taken to be

$$b^{(\mathrm{ex})} = b^{(\mathrm{in})},$$
$$H^{(\mathrm{ex})} = H^{(\mathrm{in})}, \text{ and}$$
$$\mathbf{q}^{(\mathrm{ex})} = (0.75, 0)^T$$

for this test case. Both issues need to be further investigated.

As was the case during maximum ebb, the cross-stream flow features are better resolved when p is increased to at least one, and they are very well-resolved when p is increased to two, which successfully captures the more complex features. Specifically, consider the flow between the jetties: the maximal speed occurs at two locations in this region, compared to just one when $p = 1$. Obviously, this phenomenon occurs during the outgoing tide as well, but is not quite as easily discerned in Fig. 20(c) because we are not quite at maximum ebb. Again, these results agree with those presented in [16], and the presence of multiple local maxima in $\|\mathbf{u}\|_2$ suggest the presence of multiple local maxima in b as well. This is indeed the case, and may be spotted in Fig. 19(c). Thus, the corresponding bed profile may be thought of as possessing a dual–dual scour hole arrangement, rather than simply a dual setup as seen in Fig. 19(b).

4.5. Parallel performance

We conclude this section with some brief remarks on the performance aspect of the model in parallel. The numerical results presented in the previous three sections have focused on the improved accuracy in $\mathbf{w}_h$ with increasing p. However, this improvement in accuracy comes with the price of additional computational costs as p is increased. For example, increasing p from zero to one triples the number of degrees of freedom, and, in the case of the converging channel with the coarse grid, requires twice as many time steps. Also, additional computational work is needed to evaluate the interior and edge integrals, as more quadrature points are required. We attempt to quantify the amount of extra work required in the test case that follows.

Consider once again the converging channel test case described in Section 4.2. For this trial, only the coarse grid is considered. Our objective is to measure the relative CPU times when the model is run for $p = 0$, 1, and 2. We run the model using the same parameters as described in Section 4.2, except that the model is run for 1 day, instead of 90 days. For each run, 4 processors were utilized,

Table 2
Relative computational costs for solving the converging channel test case out to 1 day, using the coarse grid and 4 processes.

p	Δt (s)	SSP (s, k)	CPU time (s)	Ratio
0	1.50	1, 1	24.56	1.00
1	0.75	2, 2	139.40	5.68
2	0.50	3, 3	394.42	16.06

on a Dell PowerEdge cluster located at the Institute for Computational Engineering and Sciences (ICES) at The University of Texas at Austin (`bevo2`, for specifications visit the ICES web page www.ices.utexas.edu).

The results of these three model runs are shown in Table 2. As can be observed there, using piecewise linear basis functions instead of piecewise constant ones results in a nearly sixfold increase in CPU time, and using piecewise quadratic basis functions leads to a sixteen-fold increase. Both values are well below estimates which account for increases in the number of degrees of freedom, Runge–Kutta stages, time steps, and quadrature points. Since the run-time optimization process is complex, this phenomenon requires additional investigation; the reader is cautioned that the results shown here are preliminary; a much more thorough scaling and performance analysis will follow in a future paper.

5. Conclusions

In this paper, a well-balanced (as demonstrated in [14]) DG morphological model was implemented within the ADCIRC modeling framework by following an extended approach which specially treats the non-conservative products through the addition of stabilizing terms in the numerical flux. An investigation of the resulting RKDG method was made, and it was verified that the scheme maintains first- through fourth-order accuracy away from shocks prior to their formation, provided that the mesh is sufficiently h-refined in the shock vicinity; the theoretical convergence rates were nearly attained in these cases.

Effects of h- and p-refinement were readily seen in the test cases: numerical solutions appeared to converge to those with the lowest values of h and highest values of p, with the highly-refined approximations able to capture subgrid-scale features, especially in the transition regions near scour hole boundaries. Moreover, it was observed that sufficient p-refinement (and to a lesser extent, sufficient h-refinement) is necessary for the accurate computation of sediment transport rates. That is, very low-order p approximations resulted in artificially low sediment pick-up, even with highly amplified transport formulæ, and the method appeared to be too diffusive. This latter point must be emphasized: since finite volume models are in fact equivalent to DG models with $p = 0$, the numerical results in Section 4 suggest that FV-based models can yield poorly-resolved sediment solutions.

Although it is clear that a three-dimensional model is required to accurately resolve all the flow features around structures such as bridge piers, it was discovered that this morphological model does capture a surprising number of complex flow characteristics, including those of the wake, scour hole shape and location, accretion region, and points of flow separation.

Lastly, it was demonstrated that the use and selection of a slope limiter plays a crucial role in improving the solution quality in these cases. This was especially true for higher-order approximations, as its omission resulted in significant spurious oscillations in the solution, and even instability in some extreme cases. Inclusion of a higher-order slope limiter is therefore critically important for DG morphological models which accommodate arbitrary-order solution approximation.

References

[1] US Army Corps of Engineers. <http://www.usace.army.mil/services/Pages/Services.aspx>.
[2] M.B. Collins, P.S. Balson, Coastal and Shelf Sediment Transport: An Introduction, in: P.S. Balson, M.B. Collins (Eds.), Coastal and Shelf Sediment Transport, London, 2007.
[3] L. Fraccarollo, H. Capart, Y. Zech, A Godunov method for the computation of erosional shallow water transients, Int. J. Numer. Meth. Fluids 41 (2003) 951–976.
[4] F.M. Exner, Über die Wechselwirkung zwischen Wasser und Geschiebe in Flüssen, Sitzber. Akad. Wiss. Wien 134 (Abt. IIa) (1925) 165–203 (in German).
[5] Z. Cao, G. Pender, S. Wallis, P. Carling, Computational dam-break hydraulics over erodible sediment bed, J. Hydraul. Engrg. 130 (2004) 689–703.
[6] V. Caleffi, A. Valiani, A. Bernini, High-order balanced CWENO scheme for movable bed shallow water equations, Adv. Water Resour. 30 (2007) 730–741.
[7] M.J. Castro Díaz, E.D. Fernández-Nieto, A.M. Ferreiro, Sediment transport models in shallow water equations and numerical approach by high order finite volume methods, Comput. Fluids 37 (2008) 299–316.
[8] X. Liu, B.J. Landry, M.H. García, Two-dimensional scour simulations based on coupled model of shallow water equations and sediment transport on unstructured meshes, Coastal Engrg. 55 (2008) 800–810.
[9] G. Simpson, S. Castelltort, Coupled model of surface water flow, sediment transport and morphological evolution, Comput. Geosci. 32 (2006) 1600–1614.
[10] J. Hudson, P.K. Sweby, Formulations for numerically approximating hyperbolic systems governing sediment transport, J. Sci. Comput. 19 (2003) 225–252.
[11] J. Hudson, P.K. Sweby, A high-resolution scheme for the equations governing 2D bed-load sediment transport, Int. J. Numer. Meth. Fluids 47 (2005) 1085–1091.
[12] W. Long, J.T. Kirby, Z. Shao, A numerical scheme for morphological bed level calculations, Coastal Engrg. 55 (2005) 167–180.
[13] P.A. Tassi, S. Rhebergen, C.A. Vionnet, O. Bokhove, A discontinuous Galerkin finite element model for river bed evolution under shallow flows, Comput. Meth. Appl. Mech. Engrg. 197 (2008) 2930–2947.
[14] S. Rhebergen, O. Bokhove, J.J.W. van der Vegt, Discontinuous Galerkin finite element methods for hyperbolic nonconservative partial differential equations, J. Comp. Phys. 227 (2008) 1887–1922.
[15] V. Aizinger, C. Dawson, The local discontinuous Galerkin method for three-dimensional shallow water flow, Comput. Meth. Appl. Mech. Engrg. 196 (2007) 734–746.
[16] E.J. Kubatko, Development, Implementation, and Verification of hp-discontinuous Galerkin Models for Shallow Water Hydrodynamics and Transport, Ph.D. Dissertation, University of Notre Dame, 2005.
[17] S. Bunya, E.J. Kubatko, J.J. Westerink, C. Dawson, A wetting and drying treatment for the Runge–Kutta discontinuous Galerkin solution to the shallow water equations, Comput. Meth. Appl. Mech. Engrg. 198 (2009) 1548–1562.
[18] E.J. Kubatko, J.J. Westerink, C. Dawson, hp Discontinuous Galerkin methods for advection dominated problems in shallow water flow, Comput. Meth. Appl. Mech. Engrg. 196 (2006) 437–451.
[19] E.J. Kubatko, J.J. Westerink, C. Dawson, Semi-discrete discontinuous Galerkin methods and stage exceeding order strong stability preserving Runge–Kutta time discretizations, J. Comp. Phys. 222 (2007) 832–848.
[20] E. Kubatko, S. Bunya, C. Dawson, J.J. Westerink, Dynamic p-adaptive Runge–Kutta discontinuous Galerkin methods for the shallow water equations, Comput. Methods Appl. Mech. Engrg. 198 (2009) 1766–1774.
[21] E.J. Kubatko, C. Dawson, J.J. Westerink, Time step restrictions for Runge–Kutta discontinuous Galerkin methods on triangular grids, J. Comp. Phys. 227 (2008) 9697–9710.
[22] E.J. Kubatko, S. Bunya, C. Dawson, J.J. Westerink, C. Mirabito, A performance comparison of continuous and discontinuous finite element shallow water models, J. Sci. Comput. 40 (2009) 315–339.
[23] S. Bunya, J.C. Dietrich, J.J. Westerink, B.A. Ebersole, J.M. Smith, J.H. Atkinson, R. Jensen, D.T. Resio, R.A. Luettich, C. Dawson, V.J. Cardone, A.T. Cox, M.D. Powell, H.J. Westerink, H.J. Roberts, A high-resolution coupled riverine flow, tide, wind, wind wave and storm surge model for Southern Louisiana and Mississippi: Part I – Model development and validation, Mon. Weather Rev. 138 (2010) 345–377, doi:10.1175/2009MWR2906.1.
[24] J.C. Dietrich, S. Bunya, J.J. Westerink, B.A. Ebersole, J.M. Smith, J.H. Atkinson, R. Jensen, D.T. Resio, R.A. Luettich, C. Dawson, V.J. Cardone, A.T. Cox, M.D. Powell, H.J. Westerink, H.J. Roberts, A high-resolution coupled riverine flow, tide, wind, wind wave and storm surge model for Southern Louisiana and

Mississippi: Part II – Synoptic description and analyses of Hurricanes Katrina and Rita, Mon. Weather Rev. 138 (2010) 378–404, doi:10.1175/2009MWR2907.1.

[25] E.J. Kubatko, J.J. Westerink, C. Dawson, An unstructured grid morphodynamic model with a discontinuous Galerkin method for bed evolution, Ocean Model. 15 (2006) 71–89.

[26] G. Dal Maso, P.G. LeFloch, F. Murat, Definition and weak stability of nonconservative products, J. Math. Pures Appl. 74 (1995) 483–548.

[27] B. Camenen, M. Larson, A general formula for non-cohesive bed load sediment transport, Estuarine Coastal Shelf Sci. 63 (2005) 249–260.

[28] N. Črnjarić-Žic, S. Vuković, L. Sopta, Extension of ENO an WENO schemes to one-dimensional sediment transport equations, Comput. Fluids 33 (2004) 31–56.

[29] C. Berthon, B. Braconnier, B. Nkonga, Numerical approximation of a degenerated non-conservative multifluid model: relaxation scheme, Int. J. Num. Meth. Fluids 48 (2005) 85–90.

[30] I. Toumi, A weak formulation of Roe's approximate Riemann solver, J. Comp. Phys. 102 (1992) 360–373.

[31] A. Harten, P.D. Lax, B. van Leer, On upstream differencing and Godunov-type schemes for hyperbolic conservation laws, SIAM Rev. 25 (1983) 35–61.

[32] C.B. Vreugdenhil, Numerical Methods for Shallow-Water Flow, Kluwer, Dordrecht, 1994.

[33] M. Dubiner, Spectral methods on triangles and other domains, J. Sci. Comput. 6 (1991) 345–390.

[34] C.-W. Shu, S. Osher, Efficient implementation of essentially non-oscillatory shock-capturing schemes, J. Comp. Phys. 77 (1988) 439–471.

[35] B. Cockburn, C.-W. Shu, TVB Runge–Kutta local projection discontinuous Galerkin finite element method for conservation laws II: general framework, Math. Comp. 52 (1989) 411–435.

[36] Z. Xu, Y. Liu, C.-W. Shu, Hierarchical reconstruction for discontinuous Galerkin methods on unstructured grids with a WENO-type linear reconstruction and partial neighboring cells, J. Comp. Phys. 228 (2009) 2194–2212.

[37] Texas Advanced Computing Center, Lonestar User Guide. <http://services.tacc.utexas.edu/index.php/lonestar-user-guide>.

[38] UNESCO, Background papers and supporting data on the International Equation of State of Seawater 1980, UNESCO Technical Papers in Marine Science 38, 1981.

[39] W. Huang, Q. Yang, H. Xiao, CFD modeling of scale effects on turbulence flow and scour around bridge piers, Comp. Fluids 38 (2009) 1050–1058.

[40] S. Dey, Sediment pick-up for evolving scour near circular cylinders, Appl. Math. Model. 20 (1996) 534–539.

[41] J. Unger, W.H. Hager, Down-flow and horseshoe vortex characteristics of sediment embedded bridge piers, Exp. Fluids 42 (2007) 1–19.